

Swept-wing boundary-layer receptivity to surface non-uniformities

By V. R. GAPONENKO¹, A. V. IVANOV¹,
Y. S. KACHANOV¹ AND J. D. CROUCH²

¹Institute of Theoretical and Applied Mechanics, Novosibirsk, Russia

²Boeing Commercial Airplane Group, Seattle, USA

(Received 13 October 2000 and in revised form 22 December 2001)

The linear receptivity of a swept-wing three-dimensional boundary layer is studied experimentally and theoretically. Cross-flow instability normal modes are excited by means of surface vibration or roughness perturbations. The resulting disturbances are investigated, and the normal modes are linked to the source perturbations. Experiments are performed under controlled disturbance conditions with a time-harmonic source that is localized in the spanwise direction. A localized surface vibration is used to excite wave trains consisting of cross-flow instability waves. Normal oblique modes (harmonic in time and space) are obtained by Fourier decomposition of the wave trains. This provides the spatial variation of the normal modes and, in particular, the initial amplitudes and phases of the modes at the source location. The shape of the surface vibrator is measured and used to determine the complex receptivity coefficients for the normal modes (i.e. for various spanwise wavenumbers, wave propagation angles, and disturbance frequencies—including zero frequency). The experimental receptivity coefficients are independent of the specific shape of the surface non-uniformities and can be directly compared with calculations. The theoretical work is based on a linear approximation to the disturbance source—valid for small forcing amplitudes. Like earlier studies on roughness-induced receptivity, the basic flow is locally assumed to satisfy the parallel-flow approximation. The modal response for the cross-flow instability is determined from the residue associated with the least-stable eigenmode.

A detailed quantitative comparison between the experimental and theoretical receptivity characteristics is carried out. Good agreement is found for the roughness–vibrational receptivity coefficients of the swept-wing boundary layer (especially for the most-unstable cross-flow modes) over a range of disturbance frequencies and spanwise wavenumbers. The theory correctly predicts the initial spectra for the travelling and stationary cross-flow instabilities excited by the surface vibrations and surface roughness, respectively. The good agreement between theory and experiment suggests that the linear receptivity theory can be used effectively in engineering methods for transition prediction. The experimental data can also be used for validation of other theoretical approaches to the problem.

1. Introduction

The present study considers the three-dimensional boundary layer on a swept wing in the region of flow acceleration. The problem of turbulence onset in three-dimensional boundary layers has been investigated rather intensively in recent years

because of its fundamental and practical importance (for reviews see Kohama 1987; Zhigulyov & Tumin 1987; Reed & Saric 1989; Bippes 1990, 1999; Arnal, Casalis & Juillen 1990; Saric 1994; Kachanov 1996; and others). There are several kinds of instability in the swept-wing boundary layer, which are caused by different physical mechanisms and excite different eigenmodes of the flow. The cross-flow instability represents one of the most important, and this is the focus of the present study.

Under relatively quiet flow conditions, the boundary-layer transition location on aircraft bodies and wings depends on four main factors: (i) the spectra of most dangerous environmental disturbances, (ii) the receptivity coefficients, (iii) the boundary-layer stability characteristics, and (iv) the leading mechanisms of nonlinear disturbance interactions. These factors correspond to the four main aspects of the transition problem on swept wings. The present paper is devoted to a quantitative experimental and theoretical investigation of aspect (ii).

Although there is a large amount of previous experimental work devoted to swept-wing boundary-layer instabilities (both stationary and travelling cross-flow modes), the work on the receptivity problem is much more limited. A brief discussion of the state of art in this field is presented below.

In various practical situations the steady non-uniformities (roughness, waviness and so on) of an aircraft surface, as well as surface vibrations, acoustic perturbations and turbulence perturbations, seem to represent the most important sources for the instability waves. On real swept wings (which always have some surface waviness or roughness) the steady surface non-uniformities seem to dominate the generation process for cross-flow instability modes if the free-stream turbulence is not very strong. Even microscopic non-uniformities can have quite high magnitudes when compared to the boundary-layer displacement thickness. These non-uniformities can produce quite intensive instability waves resulting in a premature transition to turbulence (see e.g. Fyodorov 1988; Kachanov & Tararykin 1990; Radeztsky *et al.* 1993; Crouch 1993, 1994; Radeztsky, Reibert & Saric 1994, 1999; Takagi & Itoh 1994; Gaponenko, Ivanov & Kachanov 1996; Saric, Carrillo & Reibert 1998). In view of this, it is of great practical importance to investigate the influence that unsteady and steady surface non-uniformities have on transition. First, the receptivity coefficients of the laminar boundary layer with respect to these kinds of external disturbances must be evaluated both theoretically and experimentally.

Previous experimental investigations of the swept-wing boundary-layer receptivity to stationary surface non-uniformities (see Kachanov & Tararykin 1990) show the extreme complexity of directly obtaining the quantitative values of the linear receptivity coefficients. Even in the best low-turbulence wind tunnels, the free stream flow velocity has a slow temporal modulation (at frequencies less than 0.1 Hz) with a magnitude of about 0.3–0.5%. In the presence of such background modulation, it is almost impossible to extract the weak signal (with an amplitude of about 0.01%) attributed to the zero-frequency instability modes generated by micro-roughness when measuring close to the disturbance source. In experiments by Kachanov & Tararykin (1990) an attempt was made to increase the amplitude of the steady flow disturbance (in order to make it measurable) by means of an increased roughness height. However, this resulted in nonlinearity of the receptivity mechanism.

Despite these difficulties some significant experimental results on the roughness receptivity problem were obtained in the 1990s. Radeztsky *et al.* (1993, see also Radeztsky *et al.* 1999) showed that the excitation of the cross-flow (CF) vortices is strongly influenced by a microscopic surface roughness positioned in the vicinity of the swept-wing leading edge. Deyhle & Bippes (1996) and Reibert *et al.* (1996)

investigated the transition process induced by controlled surface roughness. However, quantitative values of the linear receptivity coefficients were not obtained in these (and other) previous experimental investigations.

The first theoretical study of the excitation of swept-wing CF-instability modes due to localized surface perturbations (stationary and non-stationary) was performed by Fyodorov (1988). Similar problems were investigated by Manuilovich (1990), Crouch (1993, 1994), Choudhari (1994), Bertolotti (1996, 2000) and Ng & Crouch (1999) using different theoretical approaches, and by Spalart (1993) and Collis & Lele (1999) using numerical simulations. Choudhari (1994) and Crouch (1993) also considered the coupling with acoustic disturbances to excite travelling modes. Bertolotti (1996) was probably the first to perform a quantitative comparison of theoretical and experimental (Deyhle & Bippes 1996) values of the CF-vortex amplitudes generated by a spanwise row of roughness elements. He used both receptivity theory and stability theory to calculate the chordwise development of the cross-flow disturbance amplitude. The experimental and theoretical amplitudes excited by the roughness were in good agreement. More recently, detailed comparisons were made between the experiments of Reibert *et al.* (1996) and the linear theory of Ng & Crouch (1999); a spanwise row of roughness elements was considered and the agreement was very good.

The current experimental investigation of CF-wave excitation by surface vibrations was initiated by Ivanov (1992) and Ivanov & Kachanov (1994*a,b*). Experimental results were obtained with the help of a new disturbance source designed and tested in the Novosibirsk group in 1991–92 for the excitation of cross-flow instability waves by means of localized surface vibrations. These works showed that surface vibrations are quite effective in generating CF-instability waves. However, the vibration receptivity coefficients were not obtained experimentally until 1994. This paper presents the significant progress made on the experimental determination of the receptivity amplitudes.

In the experimental part of the present study a new method of obtaining the roughness-receptivity coefficients was developed and applied. The method incorporates an investigation of the swept-wing boundary-layer receptivity to localized surface vibrations at several disturbance frequencies (as close to zero frequency as possible). This information is new and is important for comparison with theory at non-zero frequencies. In addition, the data obtained for various frequencies of vibration are extrapolated to zero frequency. The validity of the zero-frequency limit is discussed. Finally, coefficients for the linear receptivity to localized surface roughness are obtained experimentally for various values of the disturbance spanwise wavenumber. These coefficients are independent of the specific shape of the roughness and can be directly compared with the linear receptivity theory.

The theoretical part of the present study is carried out within the linear framework of the swept-wing boundary-layer receptivity to localized surface non-uniformities developed in previous studies (see Crouch 1993, 1994). The analysis is generalized here to allow for unsteady surface sources such as a localized vibrating membrane. All calculations are performed for the conditions of the present experiments.

2. Methods of study

2.1. Flow-field measurements

2.1.1. Wind-tunnel and experimental model

The mean flow on an initial section of a swept wing was simulated in the experiments by means of a swept plate with the pressure gradient induced by a contoured wall

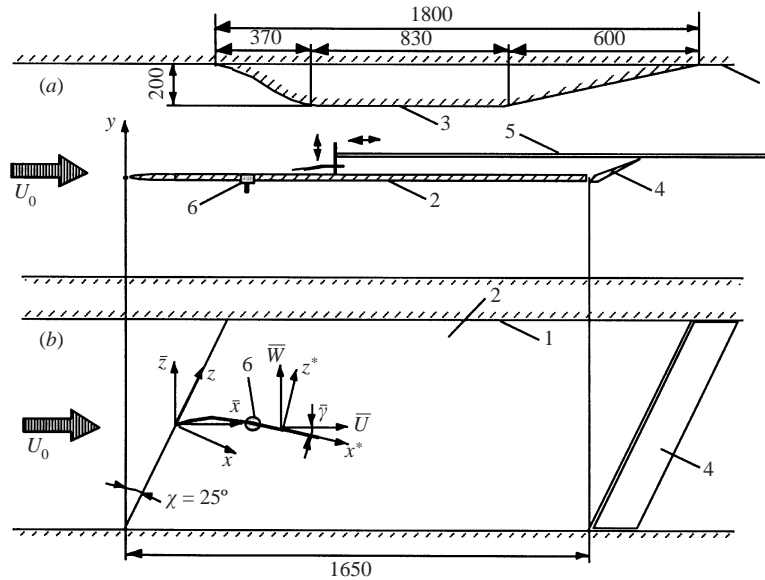


FIGURE 1. Sketch of the experimental model of the swept wing. (a) side view; (b) plan view. 1 test-section walls; 2 swept plate; 3 wall bump; 4 flap; 5 traverse; 6 localized surface vibrator.

bump mounted on the test section just above the plate (figure 1). Both the plate and the bump had the same sweep angle $\chi = 25.0^\circ$. This approach has been used in previous studies carried out by other research groups (see Saric & Yeates 1985; Nitschke-Kowsky & Bippes 1988; Müller 1990) and in our experimental group (see e.g. Kachanov, Tararykin & Fyodorov 1989, 1990; Kachanov & Tararykin 1990).

The receptivity experiments were conducted in a low-turbulence subsonic wind tunnel at the Institute of Theoretical and Applied Mechanics (Novosibirsk). The experimental model was mounted in the test section ($1 \times 1 \times 4$ m) at zero attack angle. The turbulence level ε in this wind tunnel at a free-stream velocity of about 5 to 10 m s^{-1} is usually less than 0.02% (in the frequency range higher than 1 Hz). The contoured wall bump introduced some additional disturbances into the flow, and at the conditions of the present experiments the r.m.s. value of ε (determined as $\varepsilon = u'/\bar{U}_0$) was somewhat higher, around 0.06% over the same frequency range.

The mean-flow structure and the velocity disturbances were measured by a hot-wire anemometer. The hot-wire probe was mounted on a traversing mechanism and had an accuracy of the positioning of $\Delta\bar{x} = \pm 0.1 \text{ mm}$ along the streamwise coordinate \bar{x} , $\Delta\bar{z} = \pm 0.1 \text{ mm}$ along the spanwise coordinate \bar{z} , and $\Delta y = \pm 0.005 \text{ mm}$ along the normal-to-wall coordinate y . The main coordinate systems used in the present experiments are the following (see figure 1). The coordinate system (\bar{x}, \bar{z}) is connected with the free-stream direction (upstream of the model) with the vector \mathbf{U}_0 parallel to the \bar{x} -axis. The coordinates (x, z) are aligned with the z -axis parallel to the leading edge of the model. The coordinate system (x^*, z^*) is local, such as the x^* -axis is directed along the vector \mathbf{U}_e of the potential flow near the external edge of the boundary layer. Note that for the chosen directions of the axes \bar{z} , z , and z^* , all three coordinate systems are left-handed. This choice is convenient because the corresponding two-dimensional systems, like (\bar{x}, \bar{z}) , (x, z) , and (x^*, z^*) , are right-hand systems in this case. Two additional coordinate axes are also used in this paper. The \bar{x}_e -coordinate is like the \bar{x} -coordinate, but it has its origin on the leading edge of the model (at the line

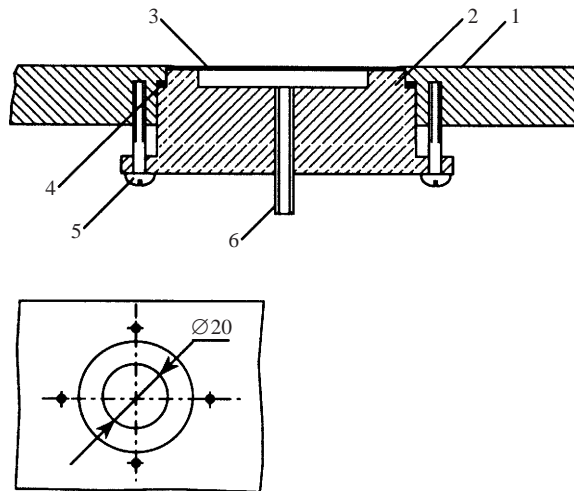


FIGURE 2. Sketch of the disturbance source (the surface vibrator). 1 surface of the model; 2 source body; 3 plastic membrane; 4 rubber washer; 5 adjusting screws; 6 outlet of pneumatic pipe.

$x = 0$). The z_c -coordinate is like the z -coordinate but it has its origin on the central line of the model $\bar{z} = 0$.

2.1.2. Excitation of disturbances

The experiments were carried out under controlled disturbance conditions. The surface non-uniformities were simulated by means of a pneumatic surface vibrator, presented in figure 2. The membrane of the source was made of a plastic film and driven by pressure fluctuations produced by a loudspeaker connected to the source by a plastic pipe (for more detail see Ivanov, Kachanov & Koptsev 1997). The source was positioned at $\bar{x} = 446$ mm, $\bar{z} = 0$ ($x = 404.2$ mm). This generator produced wave trains in the boundary layer (i.e. disturbances that are harmonic in time and localized in the spanwise direction), which consisted of the cross-flow instability modes inclined at various angles to the flow direction (see Gaponenko, Ivanov & Kachanov 1995). The wave trains were decomposed into normal oblique modes, harmonic in time and space, according to the procedure described in Gaponenko *et al.* (1995). For the case of a two-dimensional boundary layer a similar procedure is described in detail by Kachanov & Michalke (1994). After spectral decomposition, a special data-analysis procedure was applied to obtain the flow receptivity characteristics. This procedure is described below in §§ 2.2, 2.3.

2.1.3. Procedures and regimes of measurement

The measurements were made using a DISA 55M10 hot-wire anemometer and linearized by a DISA 55D10 analog linearizer. The mean value of the output voltage (i.e. the DC-component of the voltage), proportional to the \bar{x} -component of the mean flow velocity, was computer sampled. The AC-component of the voltage from the linearizer output (proportional to the \bar{x} -component of the flow velocity fluctuations) was filtered in the range from 1 Hz to 2 kHz, in order to cut off the DC-component and high-frequency instrumentation noise, respectively. Data sampling was synchronized to the signal generator used for driving the source. The disturbance frequency and amplitude were kept constant with high accuracy and measured by a frequency meter and a voltmeter. At each spatial position, four primary quantities were measured:

f (Hz)	24.8	21.43	17.9	15.0	12.0	9.02
F (at $x = 404.2$ mm)	60.7	52.4	43.6	36.5	29.5	22.2
A_{m0} (mm)	0.074	0.068	0.068	0.066	0.068	0.042
A_{m0}/δ_{1s}	0.061	0.056	0.054	0.056	0.056	0.034

TABLE 1. The six measurement regimes.

(i) the mean flow velocity, (ii) the r.m.s. intensity of the total velocity fluctuations, (iii) the phase and (iv) the r.m.s. amplitude of the velocity disturbance at the frequency of excitation.

In all regimes of excitation used for the receptivity measurements, the amplitude of the vibration was chosen to be low enough to provide linear mechanisms for the generation and development of the instability modes. This was under permanent control during the experiments. The amplitude of vibration could be varied without changing the spatial distribution of the membrane.

The main measurements in the flow were performed in the range of the chordwise coordinate $x = 438.2$ to 547.0 mm and also over the disturbance source at $x = 404.2$ mm, $\bar{z} = 0$. Six vibration frequencies were considered in the experiments, as indicated in the first row of table 1. The corresponding values of the non-dimensional frequency parameter $F = 2\pi f\nu/\bar{U}_{es}^2 \times 10^6$ are given in the second row of table 1. These frequencies are referenced to the centre of the vibrator (where ν is the kinematic viscosity of the air and $\bar{U}_{es} = 6.26 \text{ m s}^{-1}$ is the local potential flow velocity at the boundary layer edge).

For each fixed frequency, a typical data set consisted of seven spanwise (in the z -direction) distributions of velocity fluctuations measured at $x = 438.2, 456.3, 474.4, 492.6, 510.7, 528.8,$ and 547.0 mm, and a normal-to-wall profile measured over the centre of the vibrator at $\bar{x} = 446$ mm, $\bar{z} = 0$ ($x = 404.2$ mm). The spanwise distribution of the disturbance amplitude and phase was measured at a fixed non-dimensional distance from the wall corresponding to the maximum of the \bar{x} -disturbance velocity, $y_0(x) = y_{max}(x) \approx \delta_1(x)$. This distance corresponds to $\bar{U}/\bar{U}_e = 0.60$ (see Gaponenko *et al.* 1995).

2.2. Surface-vibration measurements

The membrane displacement shape during its oscillation was investigated using four different experimental techniques: (i) the laser-beam method, (ii) the hot-wire method, (iii) the hydrostatic method, and (iv) the cathetometer method. Methods (i), (iii) and (iv) were used for measurement of the membrane oscillation amplitudes, while method (ii) was used to obtain the oscillation phases. Measurements (i) and (ii) were performed inside the wind-tunnel test section simultaneously (or nearly simultaneously) with investigations of the cross-flow receptivity, while measurements (iii) and (iv) were conducted separately and aimed to check an accuracy of the laser-beam technique (i). The laser-beam method is based on measurements of the deviation of a laser beam reflected from the surface of the vibrator. The magnitude of deviation D was measured on a screen for various positions of the point of reflection along the x' -coordinate. The absolute value of the x' -coordinate was defined as $x' = \sqrt{(x - x_s)^2 - z^2}$, while the orientation of the x' -axis with respect to the x -axis was varied. Then a spatial

derivative of the amplitude of membrane oscillation $D_m = dA_m/dx'$ was determined as

$$D_m(x') = \frac{1}{2} \tan^{-1} \left(\frac{D(x')}{L} \right) \approx \frac{D(x')}{2L}, \quad (1)$$

where L is the distance along the reflected beam from the point of reflection (on the membrane surface) to the screen, and $L \gg D$. The membrane displacement was determined by means of integration as

$$A_m(x') = \int_{-R_0}^{R_0} D_m(x') dx', \quad (2)$$

where $R_0 = 10$ mm is the membrane radius.

The hot-wire method (ii) was based on hot-wire measurements in the flow over the vibrator. This method was used to determine the phase of the membrane oscillation. The normal-to-wall disturbance profile was measured at the position of the source centre ($x = 404.2$ mm, $\bar{z} = 0$). Then, the phase distribution was extrapolated to the wall by means of a curve fit in the near-wall region with a straight line. The eigenmodes excited by the vibrator in its near field have zero amplitude on the wall, while the bounded oscillations produced by the membrane displacements have a maximum on the wall, and the phase of this signal is equal to the phase of vibration plus 180° .

The hydrostatic method (iii) provided an additional measure of the membrane displacement based on fluctuations of the air volume displaced by the membrane during oscillation. This method assumes the shape of the membrane based on the laser-beam measurement. The measurements were conducted at zero frequency of oscillation simultaneous with the laser-beam measurements.

The cathetometer method (iv) is relatively simple. It is based on a direct measurement of microscopic displacement of the membrane centre during oscillation. The cathetometer is a kind of microscope (or telescope) for precise measurements of vertical displacements. These measurements were also conducted at zero frequency of vibration simultaneously with the laser-beam measurements. The accuracy of this method was estimated as ± 3 microns.

Methods (iii) and (iv) have shown that the laser-beam method gives sufficiently accurate absolute values of the membrane oscillation amplitudes.

2.3. Determining the experimental receptivity functions

The procedure for the experimental data analysis was similar to that used in previous studies of vibration receptivity performed in two-dimensional boundary layers by Ivanov *et al.* (1998), Kachanov, Koptsev & Smorodskiy (2000) and Bake *et al.* (2002).

2.3.1. Instability waves

To find the localized receptivity coefficients experimentally it was necessary to determine the initial (i.e. at the position of the surface non-uniformity) amplitudes and phases of the instability modes for every fixed value of the disturbance frequency and for various values of the spanwise wavenumber β . Due to the so-called near field, the initial complex amplitudes of the cross-flow instability modes could not be measured directly. Therefore, the amplitudes were determined in the present experiments by an upstream extrapolation of the experimental data. The experiments have shown that the normal-mode amplitudes have an almost exponential downstream behaviour, while their phases grow almost linearly. However, due to the streamwise variation of the flow and the disturbance parameters, the growth rate $-\alpha_i$ and the streamwise

wavenumbers α_r depended weakly on the streamwise coordinate x . This made the procedure for determining the initial spectral amplitudes and phases somewhat more complicated. These procedures are described in §§ 5.1 and 5.2 for the travelling cross-flow waves, and in §§ 7.1 and 7.2 for the steady cross-flow perturbations.

Measurements are made at a distance $y = y_{max}$ above the wall, where the streamwise component of the velocity perturbation is at a maximum. At the conditions of the present experiments, $y_{max} \approx \delta_1$ (the \bar{U} -profile displacement thickness), or $\bar{U}/\bar{U}_e = 0.60$. The initial spectrum of the excited instability modes measured at $y = y_{max}$ is

$$B_{1max}(\beta) \equiv B_{0max}(\beta)e^{i\phi_{0max}(\beta)}, \quad (3)$$

where $B_{0max}(\beta)$ and $\phi_{0max}(\beta)$ are the real initial amplitude and phase spectra. The complex spectrum $B_{1max}(\beta)$ can also be regarded as a function of two components of the wavevector: β and α_r . The spanwise wavenumber β is a free variable, while the chordwise wavenumber α_r depends on β according to the dispersion relationship

$$\tilde{\alpha}_r = \alpha_r(\beta). \quad (4)$$

(The tilde over α_r denotes that the streamwise wavenumber is not a free variable). The dispersion relationship (4) represents a curve in the plane (α_r, β) , while the amplitude and phase parts of the initial spectrum $B_{0max} = B_{0max}(\tilde{\alpha}_r, \beta)$ and $\phi_{0max} = \phi_{0max}(\tilde{\alpha}_r, \beta)$ represent curves in the three-dimensional spaces $(B_{0max}, \alpha_r, \beta)$ and $(\phi_{0max}, \alpha_r, \beta)$ respectively.

2.3.2. Surface vibrations

The y displacement of the membrane from an equilibrium state Y_m can be described as

$$Y_m(x', t) = f_m(x')e^{i\omega t}, \quad x' \leq R, \quad (5)$$

where R is the radius of the membrane, $\omega = 2\pi f$ is the real angular frequency of oscillation, $x' = \sqrt{x^2 + z^2}$ is a radial coordinate with its origin at the membrane centre, and $f_m(x')$ is the complex function which characterizes the shape of the membrane displacement. Note that

$$\left. \begin{aligned} f_m(x') &= A_m(x') \exp[i\phi_m(x')] & \text{at } x' \leq R, \\ f_m(x') &= 0 & \text{at } x' > R, \end{aligned} \right\} \quad (6)$$

where

$$A_m(x') = A_{m0}a_m(x') \quad (7)$$

is a real function which characterizes the amplitude of the membrane displacement during oscillation. A_{m0} is the peak amplitude of the membrane and $a_m(x')$ is a normalized amplitude function. The membrane displacement phase is written as

$$\phi_m(x') = \phi_s + \varphi_m(x'), \quad (8)$$

where ϕ_s is the phase in the centre and $\varphi_m(x')$ is a function for which $\varphi_m(0) = 0$.

Function (6) is localized in space and can be double Fourier transformed along the x - and z -coordinates using the Fourier integral. Then the complex wavenumber spectrum of the membrane vibration shape can be determined as

$$C_{m1}(\alpha_r, \beta) = \int_{-\infty}^{\infty} \int_{-\infty}^{\infty} f_m(\sqrt{x^2 + z^2}) e^{-i(\alpha_r x + \beta z)} dx dz \quad (9)$$

where

$$C_{m1}(\alpha_r, \beta) = C_m(\alpha_r, \beta) e^{i\lambda_m(\alpha_r, \beta)}, \quad (10)$$

and C_m , λ_m are real functions: C_m is the spectral amplitude and λ_m is the spectral phase.

2.3.3. Receptivity function

Following Fyodorov (1988), for every fixed frequency of vibration we can define the *complex receptivity function*

$$G_{r1}(\alpha_r, \beta) = G_r(\alpha_r, \beta)e^{i\varphi_r(\alpha_r, \beta)} \quad (11)$$

(where G_r and φ_r are real) as follows:

$$G_{r1}(\tilde{\alpha}_r, \beta) \stackrel{\text{def}}{=} \frac{B_{1\max}(\tilde{\alpha}_r, \beta)}{C_{m1}(\tilde{\alpha}_r, \beta)}, \quad (12)$$

$$G_r(\tilde{\alpha}_r, \beta) \stackrel{\text{def}}{=} \frac{B_{0\max}(\tilde{\alpha}_r, \beta)}{C_m(\tilde{\alpha}_r, \beta)}, \quad (13)$$

$$\varphi_r(\tilde{\alpha}_r, \beta) \stackrel{\text{def}}{=} \phi_{0\max}(\tilde{\alpha}_r, \beta) - \lambda_m(\tilde{\alpha}_r, \beta). \quad (14)$$

Functions $C_m(\alpha_r, \beta)$ and $\lambda_m(\alpha_r, \beta)$ represent surfaces in the three-dimensional spaces (C_m, α_r, β) and $(\lambda_m, \alpha_r, \beta)$, while functions $C_m = C_m(\tilde{\alpha}_r, \beta)$ and $\lambda_m = \lambda_m(\tilde{\alpha}_r, \beta)$ (the so-called resonant spectral modes of vibration) correspond to curves lying on these surfaces. The projections of these curves onto the plane (α_r, β) correspond to the experimentally determined dispersion curve (4).

Of course, the complex receptivity function G_{r1} depends also on the frequency f and the basic flow parameters.

2.4. Theoretical approach

The receptivity theory is based on a linear perturbation to the infinite swept-wing boundary layer considered in the experiment. We introduce a small parameter $\varepsilon = A_{m0}/\delta_{1s}$ to characterize the amplitude of the surface vibration (or height of the surface roughness). The vibrator amplitude A_{m0} is defined in §2.3.2, and the displacement thickness δ_{1s} is defined in §3.2. The total velocity satisfies the surface boundary conditions

$$u = 0, \quad v = \varepsilon \frac{\partial G}{\partial t}, \quad w = 0 \quad \text{at} \quad y = \varepsilon G(x, z, t) = \varepsilon H(x, z)e^{-i\omega t}, \quad (15)$$

where $H(x, z)$ is a function describing the vibrator-membrane shape and ω is the angular frequency of the membrane harmonic oscillation. Here the spatial coordinates are referenced to the centre of the vibrator. The velocity is decomposed into a basic-state velocity V and a perturbation velocity v_ε . The total velocity is written as

$$\mathbf{v}(x, y, z, t) = V(y) + \varepsilon v_\varepsilon(x, y, z, t). \quad (16)$$

The basic-state velocity is given by the Falkner–Skan–Cooke solution for given values of the Hartree parameter β_H and the local edge sweep angle χ_e . The parameter values are chosen to match the experiment at the location of the comparisons (generally, at the centre of the vibrator). The chordwise variation of the basic flow is neglected in the local analysis, following the parallel-flow approximation. Substituting the velocity expansion into the Navier–Stokes equations leads to the Orr–Sommerfeld and Squire equations governing the perturbation velocity (Crouch 1992, 1993). The boundary conditions are homogeneous outside the boundary layer and non-homogeneous at

the wall. For small $\varepsilon \ll 1$, the surface boundary condition can be linearized to yield

$$u_\varepsilon = -\frac{dU}{dy}H(x, z)e^{-i\omega t}, \quad v_\varepsilon = -i\omega H(x, z)e^{-i\omega t}, \quad w_\varepsilon = -\frac{dW}{dy}H(x, z)e^{-i\omega t} \quad \text{at } y = 0. \quad (17)$$

Under the parallel-flow and infinite swept-wing approximations, the coefficients in the governing equations are independent of x and z . Thus, the surface perturbation and the associated perturbation velocities are represented by Fourier integrals similar to the experimental analysis. After calculating the velocity components in Fourier space, the physical velocities are determined by integrating over α and β . For example, the u -velocity component is written as

$$u_\varepsilon(x, y, z, t) = \frac{1}{(2\pi)^2} \int_{-\infty}^{\infty} \int_{-\infty}^{\infty} \hat{u}_\varepsilon(\alpha, y, \beta, \omega) e^{i(\alpha x + \beta z)} d\alpha d\beta e^{-i\omega t}. \quad (18)$$

The integration over α is taken in the complex plane for given values of ω and β . Focusing on the modes that dominate the solution downstream, the α integral is given by the residue associated with the least-stable eigenmode $\alpha_{CF}(\beta, \omega)$. This follows the analysis for acoustic excitation of travelling cross-flow instabilities and Tollmien–Schlichting instabilities given in Crouch (1993) and Crouch (1992), respectively. These papers provide additional details about the analysis and the numerical method used to evaluate the receptivity coefficients. The complex modal disturbance amplitude at the source (for a given ω and β) is then given by

$$B(\beta, \omega) = \varepsilon K(\alpha_{CF}, \beta, \omega) \hat{H}(\alpha_{CF}, \beta). \quad (19)$$

The physical amplitude A for the harmonic source is obtained by integrating B over β . The modal amplitude B is the product of the source vibration amplitude ε , the Fourier transform of the source shape \hat{H} (evaluated at the eigenmode wavenumber α_{CF}), and the complex receptivity coefficient K . The amplitude spectra, $B(\beta)$, and the receptivity-coefficient spectra, $K(\beta)$, are the focus of the comparisons with the experiment.

Earlier studies have shown that non-parallel effects can be significant for the cross-flow instability receptivity problem (Colles & Lele 1999 and Bertolotti 2000). However, for the current experimental conditions non-parallel effects are estimated to be small. Furthermore, it is important for practical applications to assess the more simple locally parallel approach for predicting the initial cross-flow mode amplitudes. Most of the results and conclusions from the comparison with the experiment can be generalized to non-parallel analyses.

3. Properties of the basic flow and the disturbance source

The characteristics of the three-dimensional mean flow field over the experimental model were measured accurately in both the potential flow and the boundary layer using X- and V-shaped hot-wire probes. The flow field has been documented by Kachanov *et al.* (1989) and Kachanov & Tararykin (1990). In the measurement region, this flow is similar (except for wall curvature effects) to the flow over a real swept wing with a sweep angle of 25° .

3.1. Potential flow structure

The structure of the potential flow over an infinite swept wing is independent of the spanwise z -coordinate. The \bar{U} and \bar{W} velocity components and the yaw angle $\bar{\gamma}_e$ of the

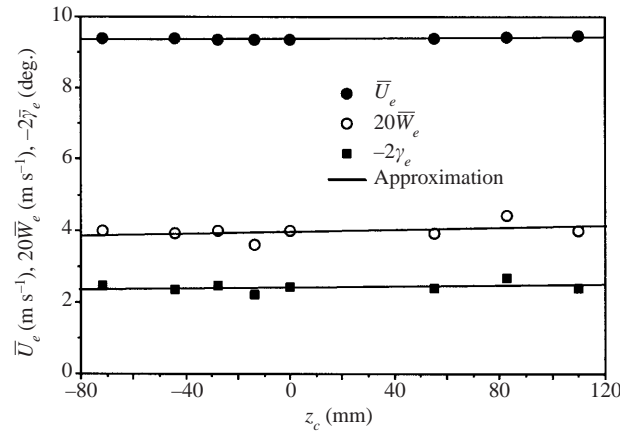


FIGURE 3. Spanwise distributions of streamwise (\bar{U}_e) and spanwise (\bar{W}_e) potential flow velocity components and yaw angle ($\bar{\gamma}_e$) of the velocity vector.

mean velocity vector at the boundary layer edge are shown in figure 3 versus z . These measurements were conducted outside the boundary layer at a distance $y = 18$ mm from the wall and $x = 427.8$ mm from the leading edge, and $\bar{U}_0 = 8.76$ m s $^{-1}$. Within experimental accuracy, all three quantities are independent of the z -coordinate. Within the primary measurement region (which lies far from the test-section sidewalls at approximately $-110 < z_c < +110$ mm), the streamwise distributions of the static pressure coefficient (C_p) and the streamwise (\bar{U}) and spanwise (\bar{W}) components of the mean velocity show little z variation (Kachanov *et al.* 1989). This testifies to the uniformity of the potential flow along the spanwise coordinate.

The experiments by Kachanov *et al.* (1989) also showed the independence (within an experimental accuracy) of the potential flow structure from the free-stream velocity \bar{U}_0 . This was measured in the region from $\bar{U}_0 = 2.8$ to 11.1 m s $^{-1}$ for $C_p(x_c)$, and from 4.74 to 8.76 m s $^{-1}$ for $U_e(x_c)$, $W_e(x_c)$ and $\gamma_e(x_c)$. Shown in figure 4(a) are the \bar{x} -distributions of the \bar{U} - and \bar{W} -components of the potential flow velocity vector measured along the central line of the model at a distance $y = \text{const.} = 18$ mm in a wide region of the downstream coordinates starting with the free stream. The streamwise dependence of the yaw angle $\bar{\gamma}_e$ is presented in figure 4(b) for several values of the \bar{z} -coordinate and for two free-stream speeds. The curve represents a polynomial approximation of all experimental points. It is seen that in the main receptivity measurement region ($483.5 < \bar{x}_c < 603.5$ mm) the yaw angle changes by less than 1° . At the position of the surface vibrator the local value of the yaw angle of the potential-flow velocity vector was $\bar{\gamma}_e = -1.17^\circ$. This corresponds to a local sweep angle $\chi_c = 25 + \bar{\gamma}_e = 23.83^\circ$.

A streamline calculated from the distributions shown in figure 4(a) is presented in figure 5. The position of the leading edge, the primary measurement regions, and the source position are also shown in figure 5 schematically. Note that the scales of the \bar{x} - and \bar{z} -axes are significantly different in this figure and the angles of turning of the streamline are not realistic (see figure 4b).

In the present experiments the free-stream velocity was $\bar{U}_0 = 6.22$ m s $^{-1}$. A streamwise distribution of the \bar{U} -component of the potential-flow velocity vector, measured at $y = 10$ mm from the model surface, is shown in figure 6. It is seen that within the main measurement region the function $\bar{U}_e(\bar{x}_c)$ is very close to a straight line (the curve shown in figure 6 represents a parabolic approximation of the experimental points).

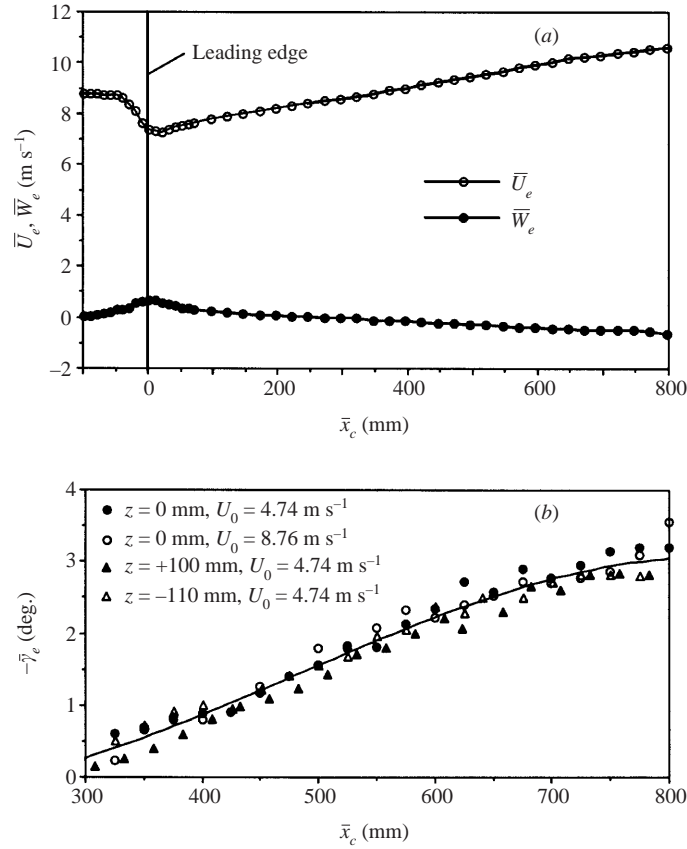


FIGURE 4. Downstream distributions of (a) streamwise (\bar{U}_e) and spanwise (\bar{W}_e) potential flow velocity components, and (b) yaw angle ($\bar{\gamma}_e$) of the velocity vector. $y = 18$ mm.

The streamwise variation of the pressure gradient parameter (Hartree parameter)

$$\beta_H = \frac{2\xi}{U_e(x)} \frac{dU_e(x)}{d\xi}, \quad \xi = \int_0^x U_e(x) dx \quad (20)$$

is also shown in figure 6. The Hartree parameter grows slowly until $\bar{x}_c \approx 600$ mm ($x \approx 543.8$ mm) and then begins to decay further downstream. At the position of the surface vibrator ($\bar{x} = 446$ mm) the local value of the Hartree parameter was $\beta_H = 0.42$.

3.2. Boundary layer structure

Typical normal-to-wall distributions of the mean-flow velocities U^* and W^* are shown in figure 7(a,b). The corresponding profiles of the yaw angle of this vector are presented in figure 7(c). The experimental points were obtained at $x = 518.4$ mm, $z = 19.3$ and 6.1 mm, $\bar{U}_0 = 8.76$ m s⁻¹. These profiles are based on slightly different conditions than those considered for the main receptivity measurements. The theoretical curves are based on the Falkner–Skan–Cooke similarity solutions for the mean flow, with $\beta_H = 0.44$ and $\chi_e = 22.9^\circ$. Very good agreement is seen between the theory and experiment, showing that the experimental and theoretical basic flows are very close to each other in the present study. Similar profiles were obtained by Fyodorov

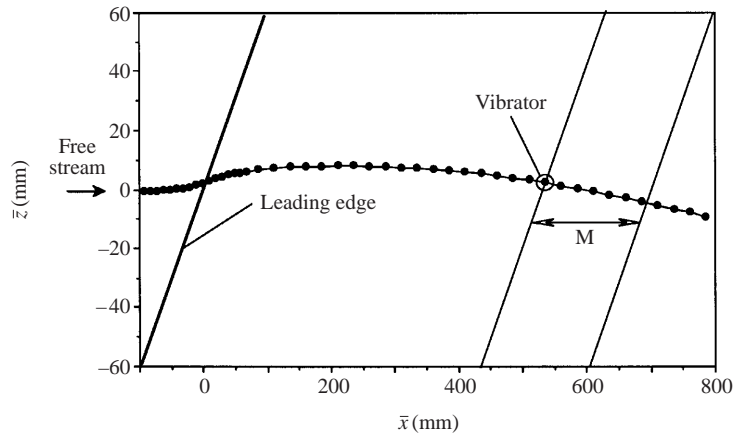


FIGURE 5. Shape of potential flow streamline. $\bar{U}_0 = 8.76 \text{ m s}^{-1}$; $y = 18 \text{ mm}$. M , region of receptivity measurements.

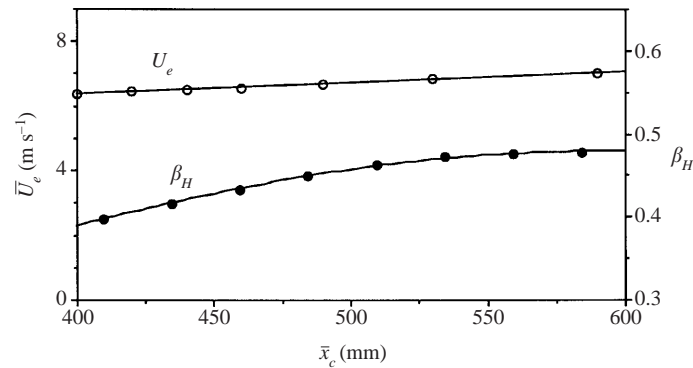


FIGURE 6. Downstream variations of the streamwise component of the potential-flow velocity (\bar{U}_e) and the Hartree parameter (β_H). $\bar{U}_0 = 6.22 \text{ m s}^{-1}$; $y = 10 \text{ mm}$.

based on the full boundary-layer equations and the experimental $\bar{U}_e(\bar{x})$ distribution and sweep condition (Kachanov *et al.* 1989).

In the present experiments a set of \bar{U} -velocity profiles was also measured in the chosen basic-flow regime at various x - and z -positions over the model. The profiles taken along the line $\bar{z} = 0$ at different streamwise positions (from $x = 404.2$ to 601.3 mm) are shown in figure 8(a). A similar set of profiles, but obtained at fixed x -coordinate ($x = 465.4 \text{ mm}$) for different spanwise positions, is shown in figure 8(b). Figure 8 shows that the form of the non-dimensional profiles is independent of spatial coordinates within the receptivity measurement region. This is corroborated by figure 9(a,b) where the streamwise and spanwise distributions of the boundary-layer displacement thickness δ_1 , momentum thickness δ_2 and the shape factor $H = \delta_1/\delta_2$ are shown together with their approximations with straight lines. All these values are essentially independent of both the \bar{x}_c - and z -coordinates. There is only a very slow downstream growth (along the \bar{x}_c -coordinate) of the displacement thickness (around 1.5% per 100 mm) and the momentum thickness (around 0.8% per 100 mm), and a very small decay of the shape factor H (around 0.6% per 100 mm). The local Reynolds number $Re = \bar{U}_e \delta_1/\nu$ grows slowly down-

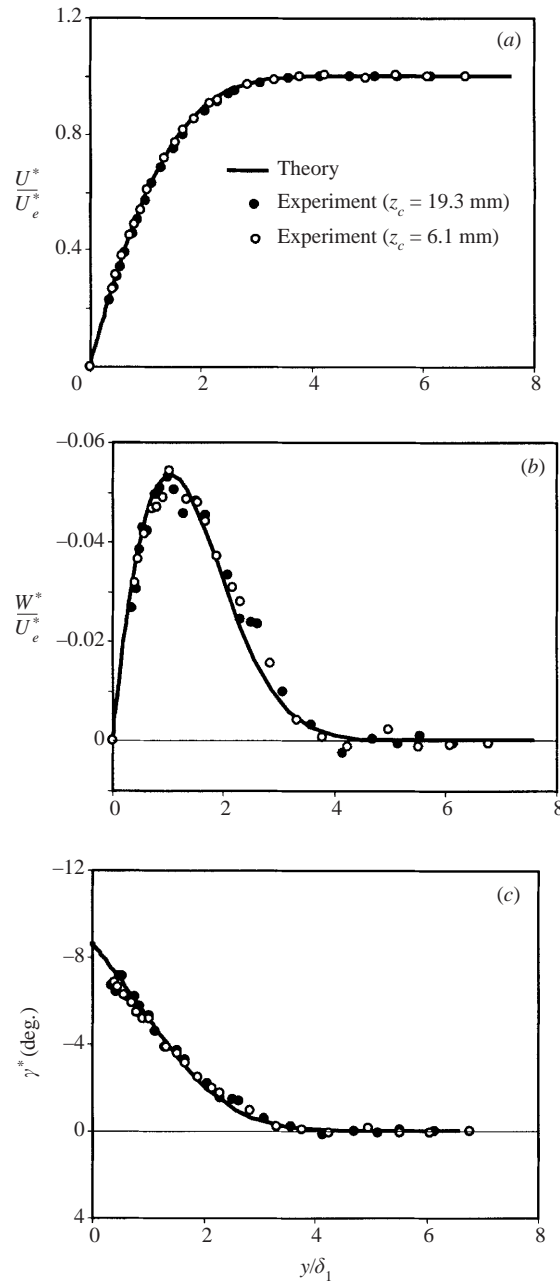


FIGURE 7. Experimental and theoretical normal-to-wall profiles for (a) the streamwise and (b) spanwise components of the mean velocity vector, and (c) its yaw angle, in the coordinate system (x^*, z^*) . $\bar{U}_0 = 8.76 \text{ m s}^{-1}$.

stream, due to the increase of \bar{U}_e in the main stream. At the centre of the surface vibrator ($\bar{x} = 446 \text{ mm}$), the boundary layer displacement thickness δ_{1s} was equal to 1.21 mm and the local Reynolds number was $Re = 498$. The parameters used for the Falkner–Skan–Cooke similarity solution at the vibrator location are $\beta_H = 0.42$ and $\chi_e = 23.8^\circ$.

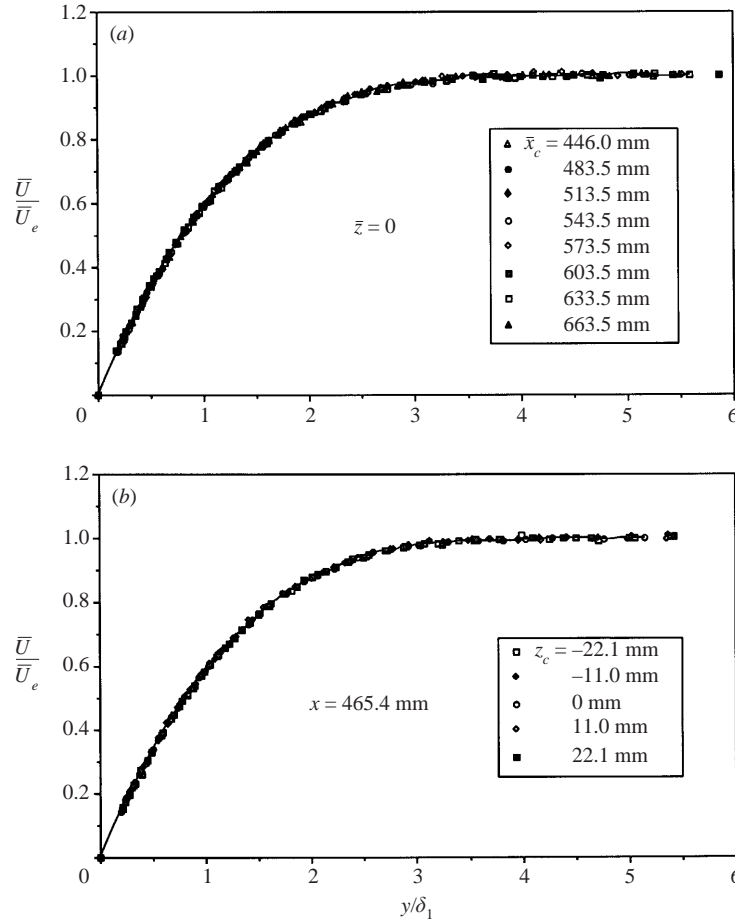


FIGURE 8. Experimental normal-to-wall profiles of the streamwise mean velocity component measured at various (a) streamwise, and (b) spanwise positions. $\bar{U}_0 = 6.22 \text{ m s}^{-1}$.

3.3. Shape of membrane oscillations

As described in §2.2, the primary measurement of the vibration shape was based on the laser-beam method for the amplitudes and the hot-wire method for the phases. These measurements were conducted both before and during the experiments in the wind tunnel. Some results of these measurements are shown in figure 10. The normalized distributions of the membrane displacement amplitudes $a_m(x')$ (see §2.3.2) were measured at various disturbance frequencies and voltage inputs. Within experimental accuracy, the shape is independent of both the frequency and the input voltage. The shape of these curves is approximated very well by an eighth-order polynomial (shown in figure 10 with a line) that is symmetric with respect to the membrane centre, and consequently, the coefficients for odd powers of x' are very close to zero. The measurements performed at various orientations of the x' -axis have shown an axisymmetry of the membrane oscillation. The polynomial presented in figure 10 (and used for Fourier decomposition of the membrane shape) had the following coefficients: $a_0 = 1.00545$, $a_1 = 0$, $a_2 = -1.744776 \times 10^{-2}$, $a_3 = 0$, $a_4 = +4.99897 \times 10^{-5}$, $a_5 = 0$, $a_6 = +3.77209 \times 10^{-7}$, $a_7 = 0$, and $a_8 = -1.334 \times 10^{-9}$, where a_n is the coefficient at x'^n for $n = 0, 1, 2, \dots$

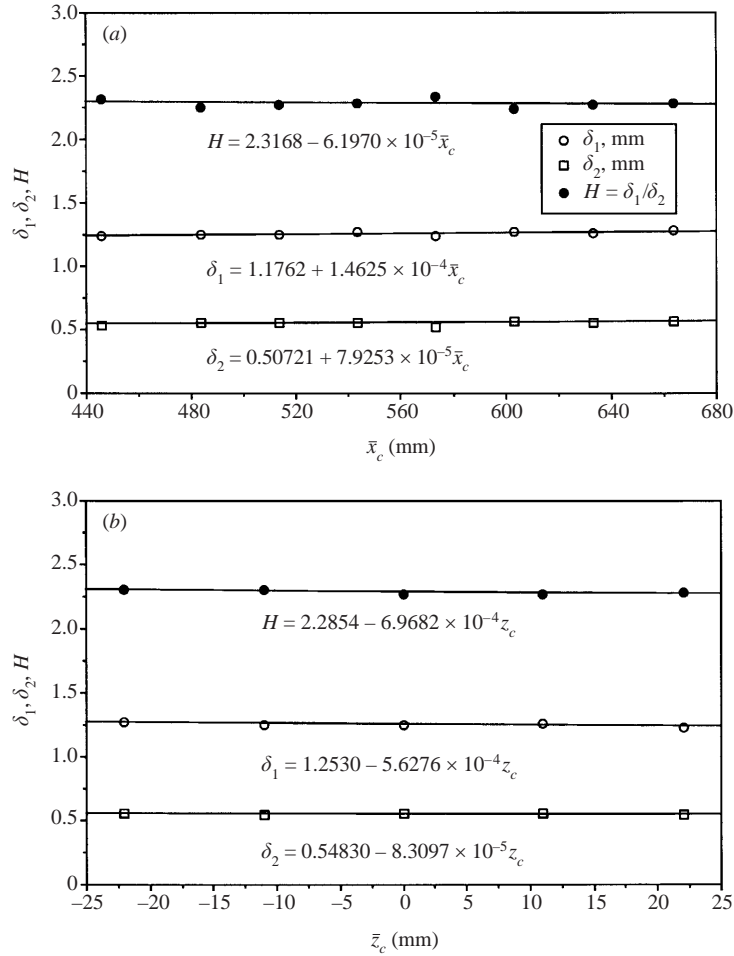


FIGURE 9. (a) Streamwise and (b) spanwise distributions of the boundary-layer displacement thickness δ_1 , the momentum thickness δ_2 and the shape factor $H = \delta_1/\delta_2$. $\bar{U}_0 = 6.22 \text{ m s}^{-1}$.

The dimensional values of the maximum amplitude of the membrane displacements A_{m0} are indicated in table 1 together with the corresponding non-dimensional amplitudes (non-dimensionalized by $\delta_{1s} = 1.21 \text{ mm}$). At these amplitudes the properties of the wave trains generated by the source were shown to be independent of the magnitude of vibration, i.e. both the receptivity and the stability mechanisms were linear. The measured phases were nearly uniform over the entire membrane.

3.4. Wavenumber spectrum of vibrations

Using the polynomial coefficients, the two-dimensional wavenumber spectrum of the membrane vibrations was determined according to the procedure described in §2.3.2. This spectrum is unique for all regimes of excitation studied in this paper because the normalized shape of the vibrations is independent of both frequency and amplitude.

Qualitatively, the general shape of this spectrum is shown in figure 11. (Only one half of this axisymmetric spectrum is plotted there.) The amplitudes are shown in logarithmic scale. The amplitude spectrum has a central cupola and side maxima ('rings') with lower magnitude (only a part of first 'ring' is seen in figure 11). The

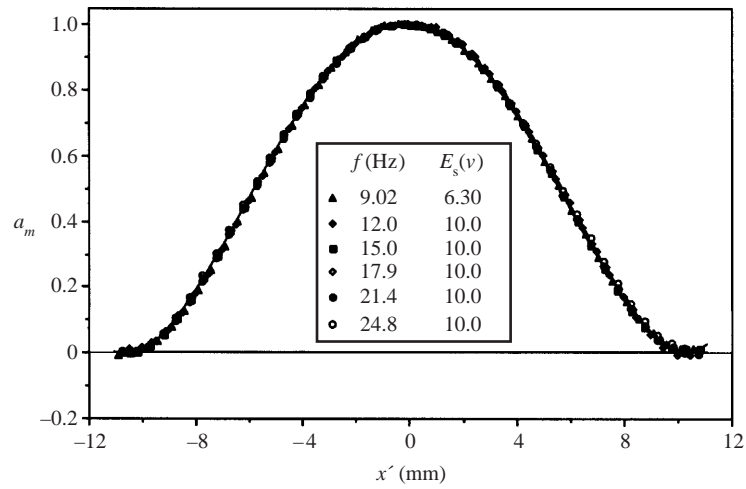


FIGURE 10. Normalized amplitude of vibration versus distance along the diameter of the membrane.

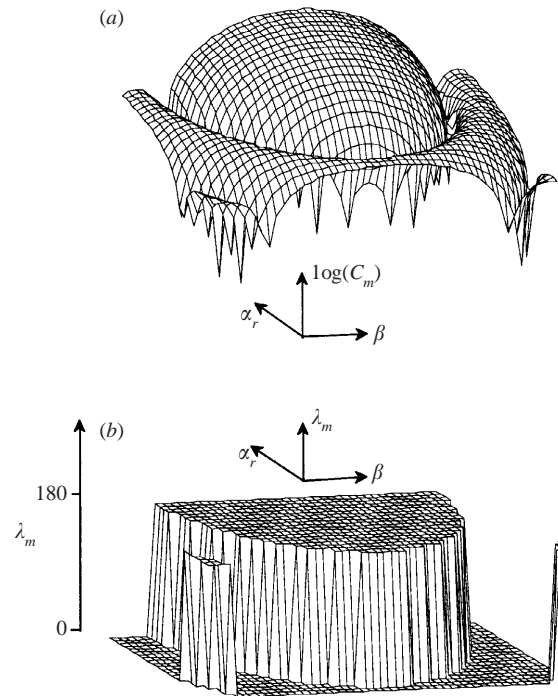


FIGURE 11. (a) Amplitude and (b) phase parts of the spectrum of the vibrator shape.

spectrum is shown in the wavenumber range $|\beta\delta_{1s}| \leq 0.8$ and $|\alpha_r\delta_{1s}| \leq 0.8$. The central cupola has a radius of about $|k\delta_{1s}| \approx 0.68$.

3.5. Resonant spectra of vibrations

The resonant modes in the two-dimensional spectrum of vibration were determined using the procedure described in §2.3.3. The 'initial' (i.e. at the source position) dispersion curves were determined experimentally for every disturbance frequency

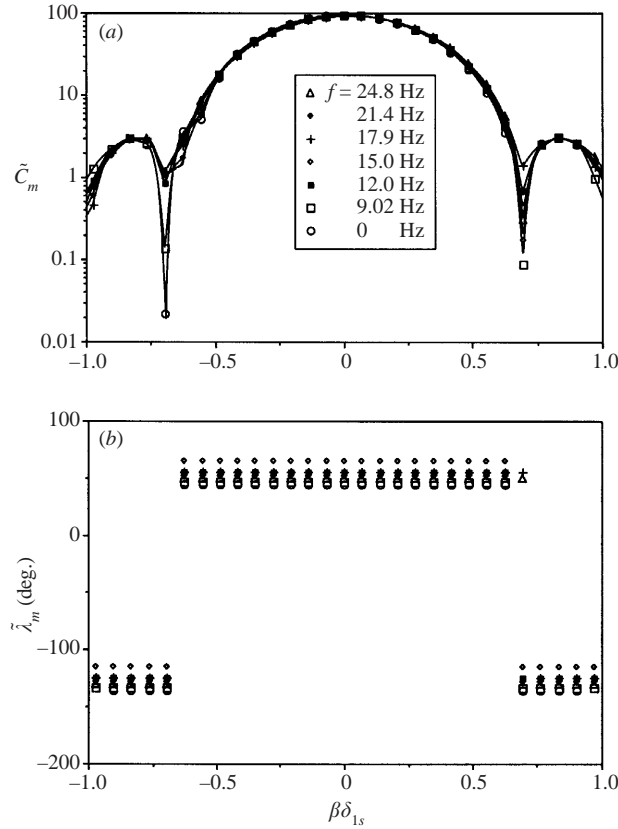


FIGURE 12. (a) Amplitude and (b) phase parts of the resonant spectra of vibrations.

(see §5.3 below). The amplitude and phase of these resonant spectra (normalized by their maximum values A_{m0}/δ_{1s}) are presented in figure 12. The amplitudes \tilde{C}_m (figure 12a) and the phases $\tilde{\lambda}_m$ (figure 12b) of spectral components are seen to be very weakly dependent on the disturbance frequency (at the present experimental conditions). The constant phase shifts between the resonant phase spectra obtained for various frequencies (figure 12b) are primarily conditioned by the method of signal generation. Two different power amplifiers and two different types of loudspeaker were used for generation of the disturbances with different frequencies. These phase differences are not important for subsequent analysis because they subtracted out. The distributions presented in figure 12 were used for determining the receptivity functions for each disturbance frequency.

4. Downstream evolution of wave trains

4.1. Spanwise distributions within wave trains

A typical set of spanwise distributions of the disturbance amplitude and phase is shown in figure 13. These quantities are measured near the maxima in the amplitude profile (at $\bar{U}/\bar{U}_e = 0.60$) for frequency $f = 24.8$ Hz, and at seven streamwise positions: $x_1 = 439.2$ mm, $x_2 = 456.3$ mm, $x_3 = 474.5$ mm, $x_4 = 492.6$ mm, $x_5 = 510.7$ mm, $x_6 = 528.8$ mm, $x_7 = 547.0$ mm (which correspond to the \bar{x} -coordinates: 483.5, 503.5, 523.5, 543.5, 563.5, 583.5, and 603.5 mm at $\bar{z} = 0$ respectively). Similar sets of spanwise distributions were obtained for other frequencies studied.

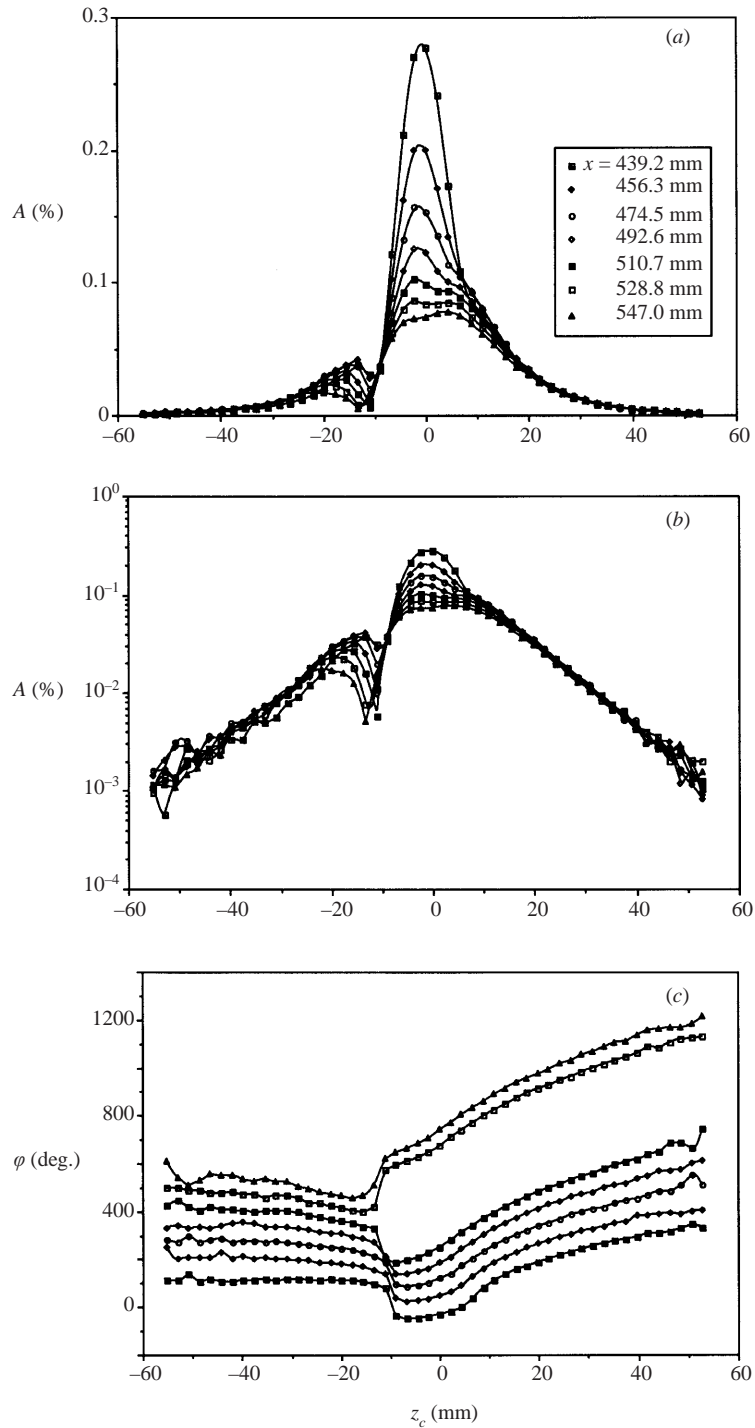


FIGURE 13. Spanwise distributions within the wave train excited by the vibrator at $f = 24.8$ Hz, and measured at seven chordwise positions: (a) amplitudes in linear scale; (b) amplitudes in logarithmic scale; (c) phases.

For all frequencies considered, the amplitude distributions are non-symmetric even though the disturbance source is symmetric. The amplitude distributions have their main maximum near the wave-train axis ($z_c = 0$) and demonstrate a quasi-exponential behaviour in their ‘tails’ (see figure 13*b*). In the range $z_c > -10$ mm (corresponding to the most powerful fluctuations) the phases grow with the z -coordinate, demonstrating that the instability modes propagating along the z -axis dominate the wave train, in agreement with previous observations (see e.g. Gaponenko *et al.* 1995).

The phase jump near $z_c \approx -10$ mm is about $\pm 180^\circ$. Between the chordwise positions $x_5 = 510.7$ mm and $x_6 = 528.8$ (for frequency $f = 24.8$ Hz) the jump changes its sign. (Similar behaviour is also observed for frequencies 21.43 and 17.91 Hz.) This phenomenon corresponds to a kind of ‘bifurcation’ of the disturbance streamline patterns in the (y, z) -plane and does not indicate any jump in the streamwise phase distributions in the range $z_c > -10$ mm. A simple shift of the phase values in this range by plus or (minus) 360° gives a gradual monotonic downstream growth of phases at any fixed spanwise position except for the vicinity of the point $z_c = -10$ mm of the ‘bifurcation’. This phase behaviour is very clear when the disturbance profiles shown in figure 13(*a, c*) are plotted in the complex plane (of real and imaginary parts of the complex disturbance amplitude) as parametric functions of the y -coordinate for different values of the x -coordinate (not shown). In such a plot, the phase ‘bifurcation’ is observed at the x -coordinate for which the line in the complex plane crosses the origin of the coordinate system. In the vicinity of the phase-jump point the disturbance amplitude is close to zero and any infinitely small change of the trajectory in the complex plane leads to a change of the phase jump direction.

Data like those shown in figure 13 represent the most important results of the measurements in the flow, which have been used for the subsequent analysis.

4.2. Wavenumber spectra of cross-flow instability modes

The amplitudes and phases of the spanwise wavenumber spectra, obtained by means of the spatial Fourier transform of the distributions shown in figure 13, are presented in figures 14(*a*) and 14(*b*) respectively. Similar sets of spectra were obtained for all other frequencies studied.

There are two distinct peaks in the amplitude spectra. They become increasingly pronounced during the downstream displacement along the chordwise coordinate x . At the frequency $f = 24.8$ Hz the peaks are located near $\beta\delta_{1s} \approx +0.22$ and -0.11 . The presence of two main maxima in the spanwise-wavenumber spectrum is a common feature observed for all frequencies. This feature is simply explained by a rapid attenuation of the quasi-two-dimensional instability modes with the spanwise wavenumbers close to zero found in previous experiments (see e.g. Gaponenko *et al.* 1995). However, the shape of the distributions shown in figure 14 is also influenced significantly by the resonant spectrum of vibrations (see §3.3 and figure 12*a*) and by the dependence of the receptivity coefficients on the spanwise wavenumber which have to be determined in the present study.

The phase part of the spectra shown in figure 14(*b*) is very flat initially (at $x = 439.2$ mm) with some phase jumps near the points $\beta\delta_{1s} \approx +0.7$ and -0.6 . This observation is consistent with the constant phase of spectral modes in the resonant spectrum of vibrations (see §3.5 and figure 12*b*) and suggests a rather weak dependence of the receptivity phases on the spanwise wavenumber. Further downstream, the phase distributions are deformed, in general agreement with stability observations (see Gaponenko *et al.* 1995).

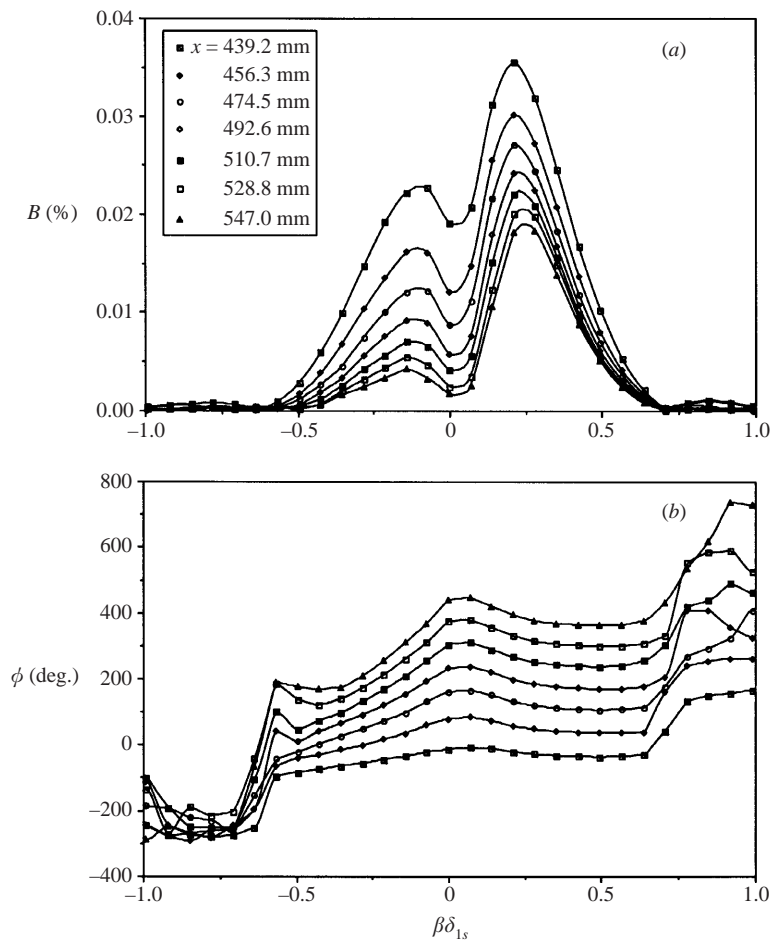


FIGURE 14. Spanwise wavenumber spectra of the wave train excited by the vibrator at $f = 24.8$ Hz, and determined at seven chordwise positions: (a) spectral amplitudes; (b) spectral phases.

5. Initial characteristics of excited cross-flow instability waves

5.1. Initial amplitude spectra of cross-flow waves; comparison of theory and experiment

According to the method of analysis described in §2.3 the initial (i.e. at the vibrator centre) amplitude spectra of the cross-flow instability modes were obtained by means of an upstream extrapolation of the spectra measured downstream of the source.

A set of streamwise distributions of logarithms of the spectral amplitudes, obtained for all frequencies at one value of the spanwise wavenumber ($\beta\delta_{1s} = 0.417$), is shown in figure 15. All these distributions are approximated (using a least-square fit) by parabolas. The downstream variation of the spectral amplitudes is quite close to exponential, but the parabolic curve fit is somewhat better. This is because the spectral modes change downstream together with the changing mean-flow parameters (i.e. the Hartree parameter, the local Reynolds number and the local sweep angle). The parabolic approximation was used for determining the initial spectra of the cross-flow instability waves.

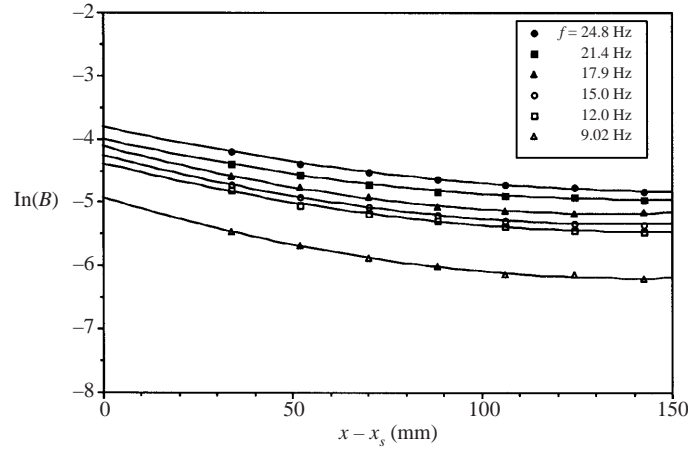


FIGURE 15. Logarithms of normal-mode amplitudes versus chordwise distance from the vibrator obtained for all studied frequencies at $\beta\delta_{1s} = 0.417$.

The initial amplitudes at the source position $B_{0max}(\beta, f) \equiv B(x_s)$ were determined as

$$\ln[B(x_s)] = \ln[B_p(x_i)] - (x_i - x_s)[\partial(\ln B_p)/\partial x]_{x=x_i}, \quad (21)$$

where $B_p(x)$ is the parabolic approximation of the experimental points, and x_i is equal to x_1 for all disturbance frequencies except for the lowest ones. For $f = 12.0$ Hz, x_i was equal to x_2 and for $f = 9.02$ Hz to x_3 . For very low frequencies, the values of the streamwise wavenumber become very small and the near field of the source becomes extended in the streamwise direction. As a result, the positions of the points $x_1 = 439.2$ mm (for $f = 12.0$ Hz) and $x_1 = 439.2$, $x_2 = 456.3$ mm (for $f = 9.02$ Hz) become too close to the source (compared to the streamwise wavelengths of these disturbances) and could not be considered far field. For example, the frequency 24.8 Hz has a streamwise wavelength λ_x^* around 10.5 mm for $\beta\delta_{1s} = 0$, and around 16.0 mm for the waves close to the most unstable ($\beta\delta_{1s} = 0.49$), whereas for the frequency 12.0 Hz these values are 19.4 and 37.1 mm respectively, and for the frequency 9.02 Hz they are 24.4 and 44.4 mm. The latter values are comparable with the distances $x_1^* - x_s^* \approx 37$ mm and $x_2^* - x_s^* \approx 57$ mm (where x_s^* is the source position).

The results of extrapolation of the spectral amplitudes to the position of the source are shown in figure 16 where the spectra of the amplitudes B_{0max} normalized by the corresponding non-dimensional amplitudes of vibration A_{m0}/δ_{1s} are presented for all disturbance frequencies. The normalized initial spectra closely resemble the resonant spectra of vibration (see § 3.5 and figure 12a) showing, at the same time, a significant frequency dependence, in contrast to the resonant spectra.

The comparison of the experimental and theoretical initial spanwise-wavenumber spectra of the cross-flow instability waves is presented in figure 17 for three frequencies of vibration. The best agreement is observed at the lowest frequency $f = 9.02$ Hz. At higher frequencies and in a range of low values of the spanwise wavenumber $\beta\delta_{1s}$ (from 0 to about 0.2) the theory predicts somewhat greater values of the initial amplitudes compared to the experiment. However, in the range $\beta\delta_{1s} \approx 0.3$ to 0.6, which includes the most unstable cross-flow modes (see Gaponenko *et al.* 1995), the agreement between the theory and the experiment is very good in the full range of frequencies studied.

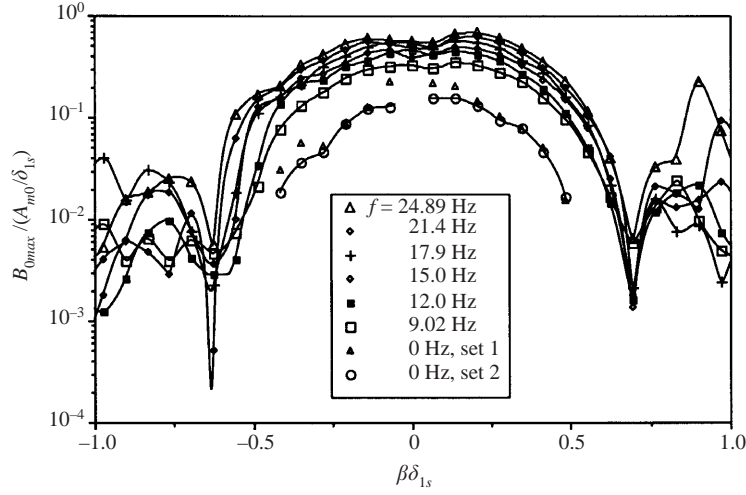


FIGURE 16. Amplitudes of initial spanwise-wavenumber spectra for cross-flow modes excited by surface non-uniformity at all studied frequencies.

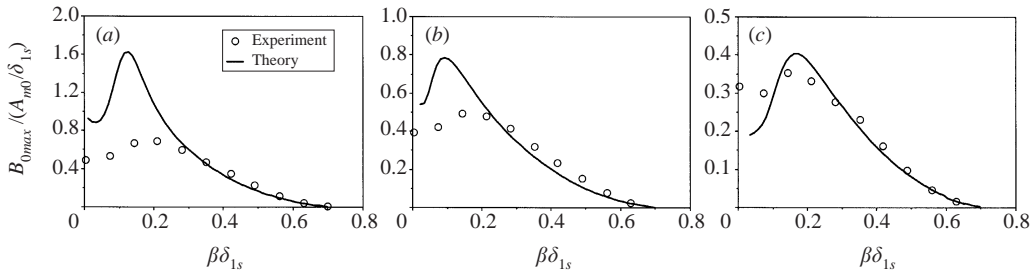


FIGURE 17. Comparison of theoretical and experimental initial spectra of cross-flow waves excited by surface vibrations. (a-c) $f = 24.8, 15.0,$ and 9.02 Hz, respectively.

5.2. Initial phase spectra of cross-flow waves

The downstream evolution of the spectral phases is shown in figure 18 for one value of the spanwise wavenumber ($\beta \delta_{1s} = 0.417$) at all frequencies. Similarly to figure 15, the distributions are approximated by parabolas that are, however, quite close to straight lines. Again the x -variation of $\partial \phi / \partial x$ is connected with the downstream change in the streamwise wavenumbers α_r , resulting from the changing mean flow. The shape of the phase distributions is almost independent of both the frequency and the spanwise wavenumber, though the slope of the curves increases with frequency.

The parabolic approximations (shown in figure 18) were used for extrapolation of the spectral-mode phases to the position of the source. According to this procedure the initial phases of spectral modes $\phi_{0max}(\beta, f) \equiv \phi(x_s)$ were determined as

$$\phi(x_s) = \phi_p(x_1) - (x_1 - x_s)(\partial \phi_p / \partial x)_{x=x_1}, \quad (22)$$

where $\phi_p(x)$ is the parabolic approximation of the experimental phase distributions.

The result of such extrapolation is shown in figure 19. The initial spectral phases $\phi_{0max} - \phi_s$ (determined with respect to the phase of oscillation measured in the membrane centre ϕ_s) have almost the same spanwise-wavenumber distributions for all frequencies. This behaviour is significantly different from that of the disturbance amplitudes (compare with figure 16).

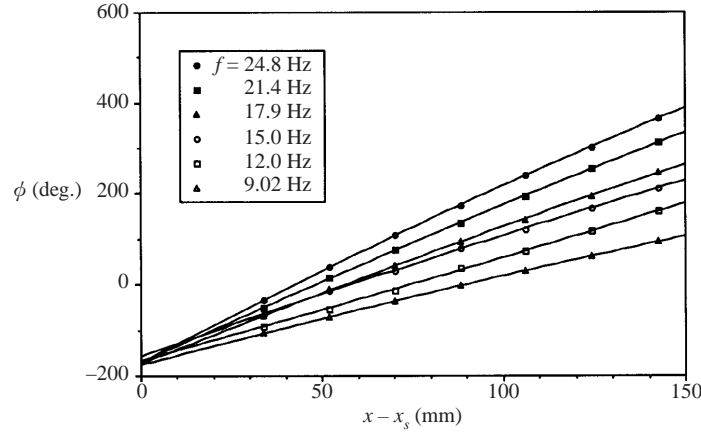


FIGURE 18. Normal-mode phases versus chordwise distance from the vibrator obtained for all studied frequencies at $\beta\delta_{1s} = 0.417$.

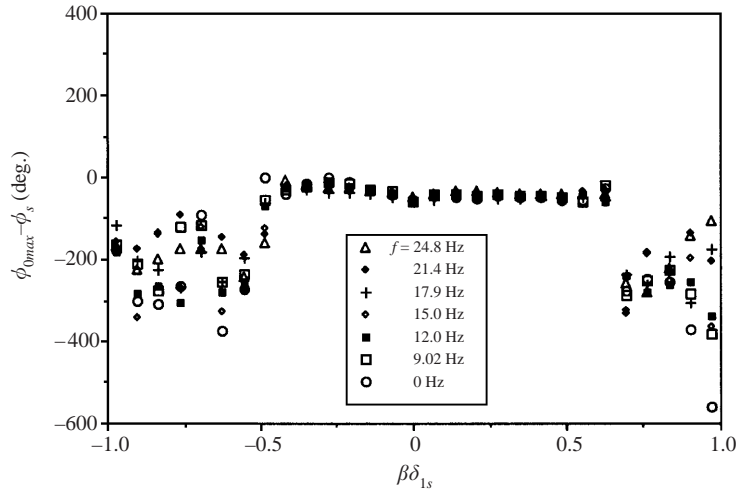


FIGURE 19. Phases of initial spanwise-wavenumber spectra of cross-flow modes excited by surface non-uniformity at all studied frequencies.

5.3. Initial dispersion functions for cross-flow waves

The initial dispersion functions $\alpha_r(\beta, x = x_s)$ of the cross-flow instability waves are needed for the selection of the resonant modes in the spectrum of vibration (see §3.5). They were obtained from experimental phase distributions like those shown in figure 18. The initial dispersion function is determined by means of a linear approximation to the functions $\phi(x)$ (for each fixed β and f) using the three x -positions closest to the source ($x_1 = 439.2$, $x_2 = 456.3$ and $x_3 = 474.5$ mm). This means that the dispersion function itself is not extrapolated. The dispersion function at the source is chosen to be the same as that of the nearest measurement station. The above assumption is substantiated by the fact that all of the $\phi(x)$ distributions show only small deviations from a straight line (see §5.2 and figure 18).

The resulting initial dispersion functions are presented in figure 20 for all frequencies. The curves shown in figure 20 have been used in the procedure for selection of the resonant modes on the two-dimensional spectrum of the vibrator (see §3.5).

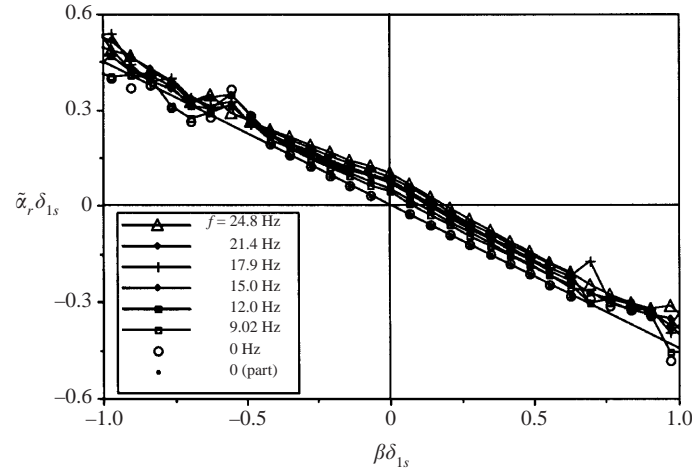


FIGURE 20. Initial dispersion functions of excited cross-flow modes for all frequencies studied.

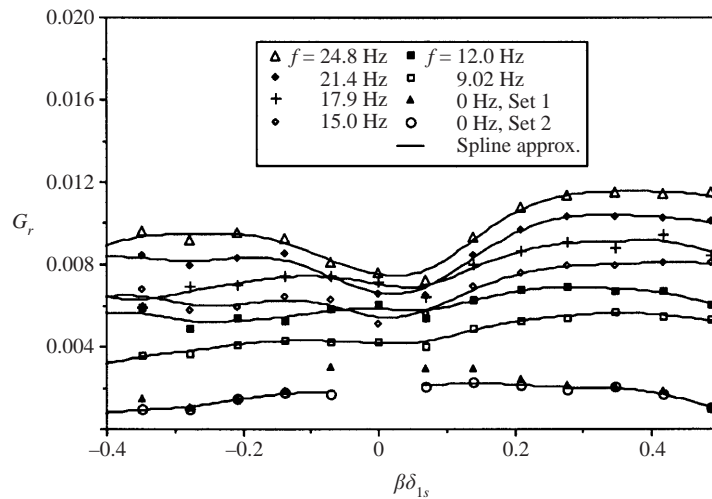


FIGURE 21. Magnitudes of the receptivity coefficient versus spanwise wavenumber for all frequencies studied.

6. Receptivity to surface vibrations

6.1. Vibration receptivity coefficients; comparison of theory and experiment

The definition of the receptivity function and the procedure for its experimental determination are presented in § 2.3. These functions were obtained experimentally for all disturbance frequencies at spanwise wavenumbers $\beta \delta_{1s}$ from -0.4 to $+0.5$ (figure 21). The latter value is very close to the most unstable cross-flow modes for all frequencies. Data were also obtained for higher absolute values of the spanwise wavenumbers but they are not reliable due to very low values of the spectral amplitudes and rather large scatter.

Figure 21 shows that the spanwise-wavenumber dependence of the receptivity coefficient becomes weaker as the frequency tends to zero, and the values of the receptivity coefficients become smaller. For high absolute values of $\beta \delta_{1s}$ the frequency dependence of the receptivity coefficients is stronger than that observed for small

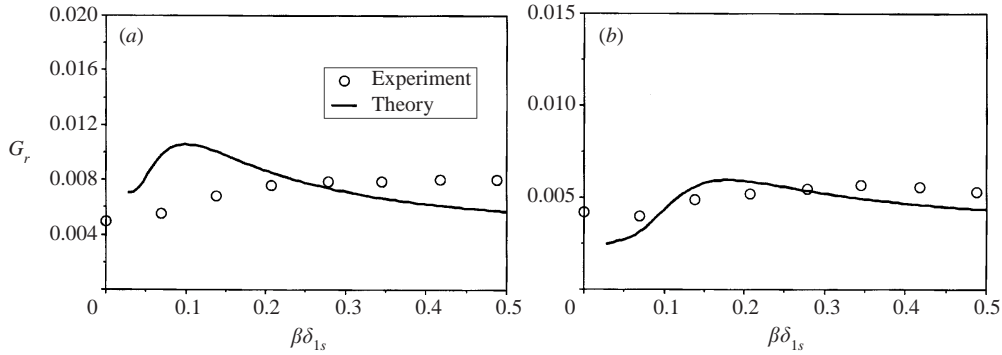


FIGURE 22. Comparison of theoretical and experimental receptivity coefficients for surface vibrations. (a) $f = 15.0$ and (b) 9.02 Hz.

values of $\beta\delta_{1s}$. Some additional properties of frequency dependence of the receptivity coefficients are discussed in § 7.

The comparison of the receptivity coefficients obtained in theory and experiment is presented in figure 22 for two frequencies of vibration $f = 15.0$ and 9.02 Hz. The experimental and theoretical values of the receptivity response functions are seen to be close to each other, especially in the range of the spanwise wavenumber corresponding to the most unstable cross-flow modes. This agreement is rather good taking into account the extreme complexity of the experimental procedure for determining the receptivity coefficients—including an extrapolation of the experimental results to the position of the source.

Note that the results presented in figures 21 and 22 are independent of the specific shape of the vibrator both in the theory and the experiment because the receptivity coefficients are obtained in Fourier space for each normal oblique mode separately.

In general, the results shown in figures 17 and 22 testify that the locally parallel receptivity theory is able to predict correctly the receptivity characteristics for surface vibrations and the initial spectra of the excited travelling cross-flow modes. The differences between the theoretical and experimental values observed for low spanwise wavenumbers is probably due to restricted accuracy of the experimental data. The finite length of the spanwise samples used in the experiment results in increased error in the spectral estimates at low wavenumbers. Non-parallel effects are another possible source of the observed differences.

6.2. Vibration receptivity phases

The phases for the complex receptivity functions were obtained as differences between the initial spectral phases of the excited cross-flow modes ϕ_{0max} (see § 5.2 and figure 19) and the phases of the corresponding modes in the resonant spectrum of the vibrator $\tilde{\lambda}_m$ (see § 3.5 and figure 12b). The result is shown in figure 23. The phase of the receptivity functions turned out to be almost independent of both the disturbance frequency and the spanwise wavenumber.

The receptivity phase characterizes a phase delay between the surface vibration and the cross-flow instability wave excited by it. The receptivity phases are important at nonlinear stages of transition on swept wings for two main reasons. First, the phase shifts influence significantly the local amplitudes of the excited disturbances, which can be very high in the case of ‘in-phase’ superposition of the generated cross-flow instability modes, and vice versa. In the case of steady cross-flow disturbances

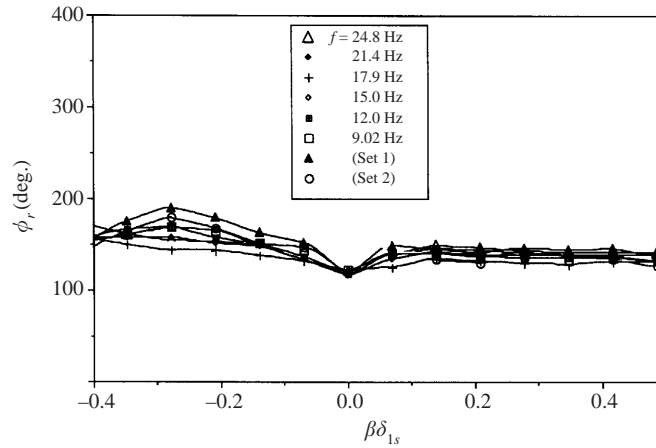


FIGURE 23. Phases of receptivity coefficients versus spanwise wavenumber for all frequencies studied.

(see §7) the ‘in-phase’ superposition can give rise (locally) to very strong high-shear layers which can accelerate the process of secondary instability and the laminar flow breakdown (see e.g. Kohama 1987). Secondly, the phase relationships between spectral modes are very important for the resonant interactions of various instability modes (see e.g. experiments by Kachanov & Levchenko 1984 for the Blasius boundary layer and Borodulin, Gaponenko & Kachanov 2000 for a swept-wing boundary layer). The resonances significantly influence the laminar–turbulent transition, and they can be efficient or not depending on the relative phase of the interacting waves.

7. Receptivity to surface roughness

The linear receptivity coefficients for localized surface roughness are determined by an extrapolation of results obtained for surface vibrations (for several frequencies close to zero) back to the zero frequency. There are several observations that justify such an approach. First, it is known from previous studies that the travelling and steady cross-flow disturbances represent physically the same type of instability modes. Second, the extrapolation of stability characteristics to zero frequency has shown good quantitative agreement with those calculated from the linear stability theory for the steady cross-flow disturbances. Third, very small frequencies of vibration, with a period $T = 1/f \gg T_b = L/\bar{U}_0$ (where T_b is a characteristic time scale of the basic flow and L is a swept-wing chord), can be regarded physically as zero frequency. The flow passes over the wing several times during a time interval when the vibrator remains practically frozen (i.e. it represents a roughness). Thus, the roughness–receptivity characteristics can be obtained experimentally by means of an extrapolation to zero frequency.

7.1. Initial amplitude spectrum of steady cross-flow modes; comparison of theory and experiment

The frequency dependence of the initial spectral amplitudes of cross-flow instability waves (normalized by the non-dimensional amplitudes A_{m0}/δ_{1s} of the membrane oscillations in its centre) is shown in figure 24 for one value of the spanwise wavenumber ($\beta\delta_{1s} = 0.417$). The data are approximated very well by a straight line. Similar behaviour was observed for other values of the spanwise wavenumber except for

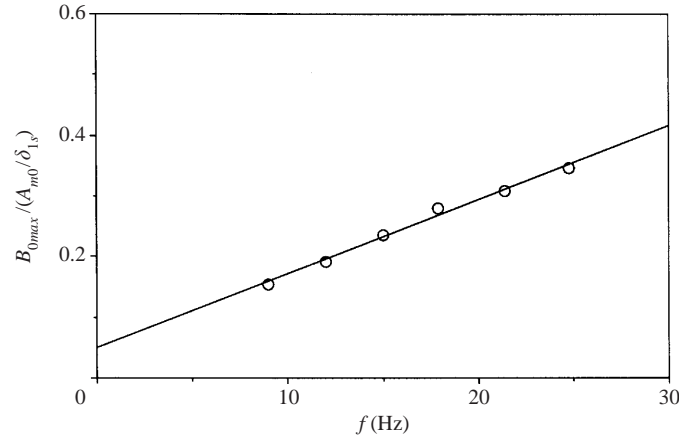


FIGURE 24. Initial amplitudes of normal cross-flow modes excited by surface non-uniformities versus frequency for $\beta\delta_{1s} = 0.417$.

quasi-two-dimensional modes with spanwise wavenumbers close to zero. Distributions like that shown in figure 24 have been used for extrapolation of the initial spectral amplitudes to the frequency $f = 0$ for all values of the spanwise wavenumber.

The results of extrapolation to the zero frequency of vibration are shown in figure 16 (together with initial spectra of disturbances obtained at non-zero frequencies). Two sets of data are given based on two evaluations of the initial spectrum. The results represent the stationary disturbance that would be produced by a surface non-uniformity of unit magnitude, having the same shape as the vibrator. The following two procedures for extrapolation to the zero frequency were used.

First, as shown in figure 24 the initial spectral amplitudes at non-zero frequencies (normalized by A_{m0}/δ_{1s}) decrease with frequency in a linear way. This fact was used for a simple linear extrapolation of initial amplitudes to the zero frequency (set 1 of points in figure 16). However, for values of the spanwise wavenumber close to zero there was larger scatter and the linear extrapolation was not satisfactory. Therefore, in these cases an extrapolation by means of a cubic spline approximation was used (set 2 of points in figure 16) along with the linear extrapolation. The points from the two sets almost coincide for most values of the spanwise wavenumber, but not for those close to zero (and not for two other points with the lowest negative values of the wavenumber shown in figure 16). Most probably, the second set of points (connected with lines) gives a better estimation of the initial spectrum of the cross-flow modes with zero frequency.

The comparison of the experimental and theoretical initial spanwise-wavenumber spectra for the steady cross-flow disturbances excited by surface roughness is presented in figure 25. In this figure the experimental amplitudes of initial spectrum are multiplied by a factor of 2 to be consistent with the standard definition of the receptivity amplitudes for steady surface non-uniformities (i.e. the zero coefficient in the Fourier series is divided by two in contrast to all other coefficients). The two sets of data for $f = 0$, discussed above, are shown in this figure. For small values of the spanwise wavenumber (approximately at $\beta\delta_{1s} < 0.16$), the theory gives lower initial amplitudes compared to the experiment. However, in this range the spanwise wavelengths become very large and the experimental uncertainty is greater. At higher values of the spanwise wavenumber, from $\beta\delta_{1s} \approx 0.2$ to 0.5 (this range includes

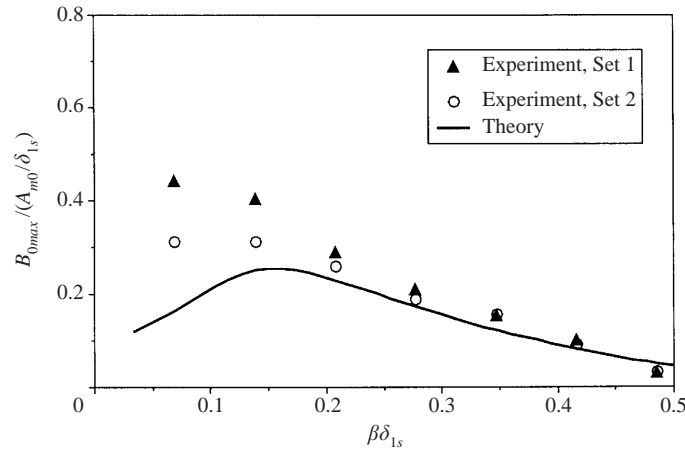


FIGURE 25. Comparison of theoretical and experimental initial spectra of stationary cross-flow modes excited by surface roughness.

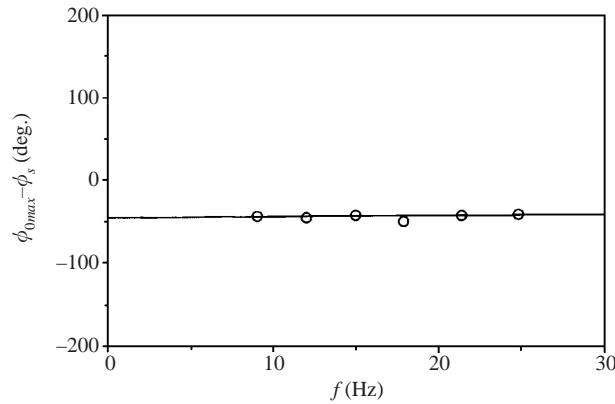


FIGURE 26. Initial phases of normal cross-flow modes excited by surface non-uniformities versus frequency for $\beta\delta_{1s} = 0.417$.

the most unstable cross-flow modes), the agreement between the theory and the experiment is very good.

7.2. Initial phase spectrum of steady cross-flow perturbations

The frequency dependence of initial phases of the cross-flow spectral modes is shown in figure 26 for the spanwise wavenumber $\beta\delta_{1s} = 0.417$. Note that the phase of the membrane vibrations ϕ_s (measured with the hot wire over the centre of the source near the membrane surface) depends weakly on the frequency. In order to take this dependence into account, the initial phases of cross-flow modes ϕ_{0max} shown in figure 26 are ‘normalized’ with the phases ϕ_s of the membrane vibrations. In contrast to the spectral phases measured at fixed positions downstream of the source (see figure 18), the ‘normalized’ initial phases $\phi_{0max} - \phi_s$ are almost completely independent of the frequency and very well approximated with a straight line. The same was observed for all other values of the spanwise wavenumber. Therefore, the extrapolation of the initial phase to the zero frequency of vibration has been performed with the help of straight lines.

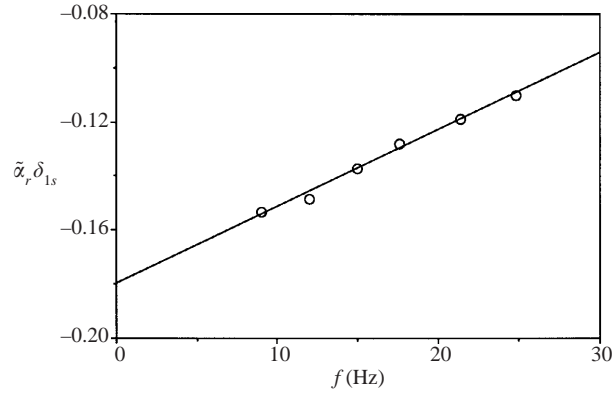


FIGURE 27. Initial streamwise wavenumber of normal cross-flow mode versus frequency for $\beta\delta_{1s} = 0.417$.

The result of the estimation of initial spectral phases $\phi_{0max} - \phi_s$ for zero frequency is shown in figure 19 together with the corresponding values for non-zero frequencies. Almost no difference is seen between the initial phases obtained for all frequencies including zero.

7.3. Initial dispersion function for steady cross-flow modes

The frequency dependence of the streamwise wavenumber $\alpha_r \delta_{1s}$ is presented in figure 27 for one of the spanwise wavenumbers ($\beta\delta_{1s} = 0.417$). For most values of the spanwise wavenumber this dependence was very well approximated with straight lines. Therefore, the initial dispersion function $\alpha_r \delta_{1s}(\beta\delta_{1s})$ for zero-frequency disturbances was estimated by means of extrapolation of the curves, like that shown in figure 27, by straight lines. The result of this extrapolation is shown in figure 20 together with the initial dispersion functions determined for the other (non-zero) frequencies. The points lying in the region of the most reliable data (from $\beta\delta_{1s} \approx -0.4$ to $\beta\delta_{1s} \approx +0.6$) are marked as black dots and approximated by a straight line. The approximation is very good, and the line nearly passes through the origin of the coordinate frame. This property is characteristic of the zero-frequency cross-flow instability modes.

To illustrate more visually the behaviour of dispersion properties of the cross-flow modes at the position of the source when the frequency tends to zero, some additional dispersion characteristics are presented in figure 28. The dependence of the wave propagation angle on the spanwise wavenumber shown in figure 28 was determined from the initial dispersion curves (see figure 20) for all disturbance frequencies including zero. When the frequency tends to zero, the dependence of θ^* on β^* becomes weaker and weaker. For zero frequency the wave propagation angle (i.e. the angle of inclination of the cross-flow vortices) becomes nearly constant. Note that the jump at $\beta^* = 0$ is not important for steady disturbances because the stationary mode does not propagate in space. The averaged values of θ^* , determined for positive and negative streamwise wavenumbers (separately), turned out to be equal to $+87.2^\circ$ and -91.3° respectively. The difference between them is close to 180° with accuracy of 1.5° . This result testifies to the reasonably high accuracy of the extrapolation of the dispersion functions to zero frequency.

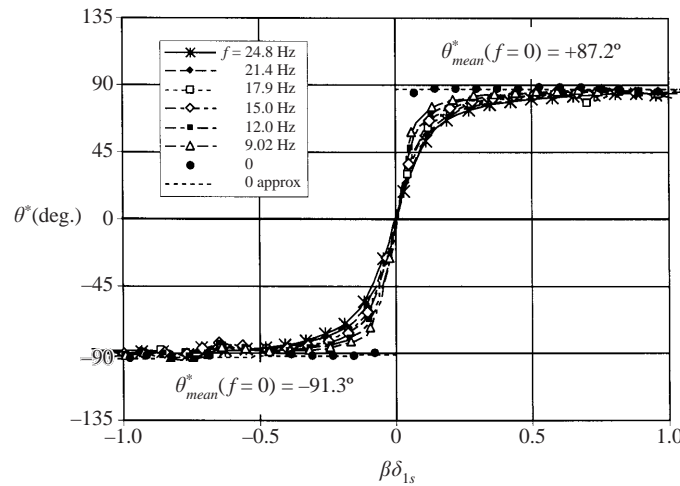


FIGURE 28. Propagation angle for cross-flow waves versus spanwise wavenumber at different frequencies.

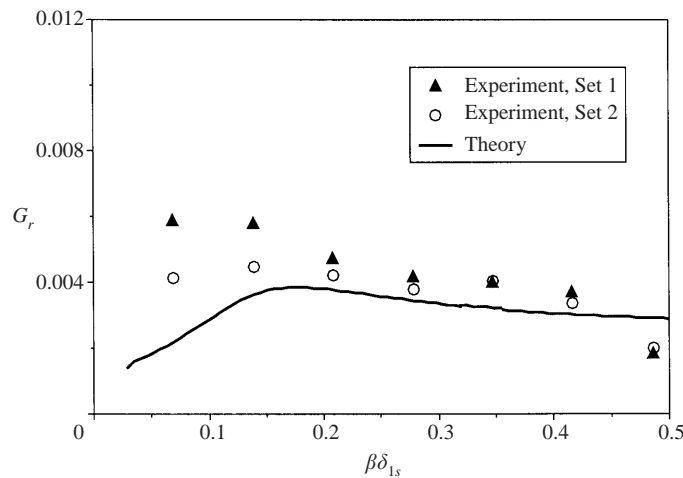


FIGURE 29. Comparison of theoretical and experimental receptivity coefficients for surface roughness.

7.4. Estimated roughness receptivity coefficients; comparison of theory and experiment

The receptivity coefficients for zero-frequency disturbances (i.e. for localized surface roughness) are presented in figure 21 together with the results obtained for the non-zero frequencies. Figure 21 shows that the receptivity amplitudes decrease with frequency in a linear way. The receptivity to localized surface non-uniformities is significantly less than that to the surface vibration. For the cross-flow waves with $\beta\delta_{1s} \approx 0.4$ (i.e. for the most unstable waves), the receptivity amplitudes found at frequency 24.8 Hz are greater than those at the zero frequency by a factor of 5 to 6. For small values of the spanwise wavenumber, this factor is around 2 to 4.

The comparison of the roughness receptivity coefficients obtained in theory and experiment is presented in figure 29. Similarly to figure 25, the experimental receptivity amplitudes shown in figure 29 are multiplied by a factor of 2 to be consistent with the standard definition of the receptivity coefficients for steady surface non-uniformities.

The two sets of data for $f = 0$, discussed above, are shown in this figure. Similarly to initial amplitude spectra of the steady cross-flow perturbations (see figure 25), the theory gives somewhat lower values at small spanwise wavenumbers (approximately at $\beta\delta_{1s} < 0.16$). At higher values, from $\beta\delta_{1s} \approx 0.2$ to 0.5, the agreement between the theory and the experiment is rather good, taking into account the restricted experimental accuracy (estimated above as $\pm 20\%$) due to the complexity of the experimental procedures. In contrast to the initial spectra shown in figure 25, the receptivity coefficients presented in figure 29 are independent of the specific shape of the roughness.

Similarly to the case of travelling waves, the results shown in figures 25 and 29 testify that the locally parallel receptivity theory is able to predict the receptivity characteristics for steady surface non-uniformities and the initial spectra of the excited steady cross-flow modes. Some differences between the theoretical and experimental values observed for low spanwise wavenumbers are partially explained by the restricted accuracy of the experimental data, but they may also result from neglecting non-parallel effects.

8. Conclusions

A combined experimental and theoretical study of swept-wing boundary-layer receptivity to localized surface vibrations and roughness has been conducted. Quantitative comparison is made between the experimental and theoretical results. The frequency dependence is obtained over a range of spanwise wavenumbers for: (i) the initial spectral amplitudes and phases of the excited cross-flow instability waves, (ii) the initial dispersion functions of instability modes, and (iii) the receptivity coefficients for the swept-wing boundary-layer subject to localized surface vibrations. An approximation for the frequency dependence of these quantities was used to extrapolate the experimental data to zero frequency. As a result the initial spectrum, the initial dispersion function, and the receptivity coefficients are evaluated experimentally for zero-frequency perturbations (i.e. for the stationary cross-flow disturbances excited by steady surface non-uniformities).

The swept-wing boundary-layer receptivity coefficients for surface vibrations and roughness, obtained in the present paper, are independent of the specific shape of the surface non-uniformities. These coefficients can be used for estimating the initial spectra of the cross-flow instability modes for any given shape of localized (in the streamwise direction) non-uniformity. The experimental results can also be used for verification of numerically simulated receptivity amplitudes.

The following main conclusions can be drawn from the results of the present study.

1. Good quantitative agreement between the experimental and theoretical results is found for localized surface perturbations. This includes receptivity amplitudes and initial amplitude spectra of the excited cross-flow instability modes over a range of spanwise wavenumbers ($\beta\delta_{1s} \approx 0.2$ to 0.5) that includes the most unstable modes for every fixed frequency. In this range the discrepancy does not exceed the experimental error. This agreement helps validate both the experimental and the theoretical approaches used in the present study. The comparisons also show that the locally parallel receptivity theory is able to correctly predict the initial cross-flow mode amplitudes (at least for the swept-wing flow investigated).

2. For the conditions of the present study, the receptivity amplitudes decrease in a linear way as the disturbance frequency tends to zero. The receptivity to surface roughness is about 3 to 5 times smaller than that to the surface vibrations investigated.

This factor is about 4 between the most unstable steady and travelling cross-flow disturbances.

3. The phases of the vibration and roughness receptivity coefficients obtained experimentally are found to be nearly independent of the disturbance frequency, and weakly dependent on the spanwise wavenumber.

This study was supported by Boeing International Inc. and the Russian Academy of Sciences.

REFERENCES

- ARNAL, D., CASALIS, G. & JUILLEN, J. C. 1990 Experimental and theoretical analysis of natural transition on 'infinite' swept wing. In *Laminar-Turbulent Transition* (ed. D. Arnal & R. Michel), pp. 311–325. Springer.
- BAKE, S., FERNHOLZ, H., IVANOV, A., NEEMANN, K. & KACHANOV, Y. 2002 Receptivity of boundary layers to three-dimensional disturbances. *Eur. J. Mech. B/Fluids* **21**, 29–48.
- BERTOLOTTI, F. P. 1996 On the birth and evolution of disturbances in three-dimensional boundary layers. In *Nonlinear Instability and Transition in Three-Dimensional Boundary Layers* (ed. P. W. Duck & P. Hall), pp. 247–256. Kluwer.
- BERTOLOTTI, F. P. 2000 Receptivity of three-dimensional boundary-layers to localized wall roughness and suction. *Phys. Fluids* **12**, 1799–1809.
- BIPPES, H. 1990 Instability features appearing on swept wing configuration. In *Laminar-Turbulent Transition* (ed. D. Arnal & R. Michel), pp. 419–430. Springer.
- BIPPES, H. 1999 Basic experiments on transition in three-dimensional boundary layers dominated by crossflow instability. *Prog. Aerospace Sci.* **35**, 363–412.
- BORODULIN, V. I., GAPONENKO, V. R. & KACHANOV, Y. S. 2000 Interaction of stationary and travelling instability modes of cross-flow in swept-wing boundary layer. *Thermophys. Aeromech.* **7**(1), 37–45.
- CHOUDHARI, M. 1994 Roughness-induced generation of crossflow vortices in three-dimensional boundary layers. *Theor. Comput. Fluid Dyn.* **6**, 1–30.
- COLLIS, S. S. & LELE, S. K. 1999 Receptivity to surface roughness near a swept leading edge. *J. Fluid Mech.* **380**, 141–168.
- CROUCH, J. D. 1992 Localized receptivity of boundary layers. *Phys. Fluids A* **4**, 1408–1414.
- CROUCH, J. D. 1993 Receptivity of three-dimensional boundary layers. *AIAA Paper* 93-0074.
- CROUCH, J. D. 1994 Theoretical studies on the receptivity of boundary layers. *AIAA Paper* 94-2224.
- DEYHLE, H. & BIPPES, H. 1996 Disturbance growth in an unstable three-dimensional boundary layer and its dependence on environmental conditions. *J. Fluid Mech.* **316**, 73–113.
- FYODOROV, A. V. 1998 Generation of the cross-flow instability waves in swept-wing boundary layer. *Zh. Prikl. Mekh. i Tekh. Fiz.* **5**, 46–52 (in Russian).
- GAPONENKO, V. R., IVANOV, A. V. & KACHANOV, Y. S. 1995 Experimental study of cross-flow instability of a swept-wing boundary layer with respect to travelling waves. In *Laminar-Turbulent Transition* (ed. R. Kobayashi), pp. 373–380. Springer.
- GAPONENKO, V. R., IVANOV, A. V. & KACHANOV, Y. S. 1996 Experimental study of 3D boundary-layer receptivity to surface vibrations. In *Nonlinear Instability and Transition in Three-Dimensional Boundary Layers* (ed. P. W. Duck & P. Hall), pp. 389–398. Kluwer.
- IVANOV, A. V. 1992 Development of a wave pocket in a boundary layer on a swept wing. Diploma Work (Master Thesis), Novosibirsk State Tech. Univ., Novosibirsk (in Russian).
- IVANOV, A. V. & KACHANOV, Y. S. 1994a A method of study of the stability of 3D boundary layers using a new disturbance generator. In *7th Intl Conf. on the Methods of Aerophysical Research. Proc. Part 1*, pp. 125–130. Novosibirsk: Inst. of Theor. & Appl. Mech.
- IVANOV, A. V. & KACHANOV, Y. S. 1994b Excitation and development of spatial packets of instability waves in a three-dimensional boundary layer. *Thermophys. Aeromech.* **1**(4), 287–305.
- IVANOV, A. V., KACHANOV, Y. S. & KOPTSEV, D. B. 1997 An experimental investigation of instability wave excitation in three-dimensional boundary layer at acoustic wave scattering on a vibrator. *Thermophys. Aeromech.* **4**(4), 359–372.
- IVANOV, A. V., KACHANOV, Y. S., OBOLENTSEVA, T. G. & MICHALKE, A. 1998 Receptivity of the

- Blasius boundary layer to surface vibrations. Comparison of theory and experiment. In *9th Intl Conf. on Methods of Aerophysical Research. Proc. Part I*, pp. 93–98, Novosibirsk: Inst. of Theor. & Appl. Mech.
- KACHANOV, Y. S. 1996 Generation, development and interaction of instability modes in swept-wing boundary layer. In *Nonlinear Instability and Transition in Three-Dimensional Boundary Layers* (ed. P. W. Duck & P. Hall), pp. 115–132. Kluwer.
- KACHANOV, Y. S., KOPTSEV, D. B. & SMORODSKIY, B. D. 2000 Suppression of 3D vibration receptivity of boundary layer by an adverse pressure gradient. In *10th Intl Conf. on Methods of Aerophysical Research. Proc. Part I*, p. 134–139, Novosibirsk: Inst. of Theor. & Appl. Mech.
- KACHANOV, Y. S. & LEVCHENKO, V. Y. 1984 The resonant interaction of disturbances at laminar-turbulent transition in a boundary layer. *J. Fluid Mech.* **138**, 209–247.
- KACHANOV, Y. S. & MICHALKE, A. 1994 Three-dimensional instability of flat-plate boundary layers: Theory and experiment. *Eur. J. Mech. B/Fluids* **13**, 401–422.
- KACHANOV, Y. S. & TARARYKIN, O. I. 1990 The experimental investigation of stability and receptivity of a swept-wing flow. In *Laminar-Turbulent Transition* (ed. D. Arnal & R. Michel), pp. 499–509. Springer.
- KACHANOV, Y. S., TARARYKIN, O. I. & FYODOROV, A. V. 1989 Experimental simulation of swept-wing boundary layer in a region of cross-flow formation. *Izv. Sib. Otd. Akad. Nauk SSSR, Tekh. Nauk.* **3**, 44–53 (in Russian).
- KACHANOV, Y. S., TARARYKIN, O. I. & FYODOROV, A. V. 1990 Investigation of stability of boundary layer on a model of a swept wing to stationary disturbances. *Izv. Sib. Otd. Akad. Nauk SSSR, Tekh. Nauk.* **5**, 11–21 (in Russian).
- KOHAMA, Y. 1987 Some expectation on the mechanism of cross-flow instability in a swept wing flow. *Acta Mechanica* **66**, 21–38.
- MANUILOVICH, S. V. 1990 Disturbances of three-dimensional boundary layer generated by surface roughness. *Fluid Dyn.* **24**, 764–769.
- MÜLLER, B. 1990 Experimental study of the travelling waves in a three-dimensional boundary layer. In *Laminar-Turbulent Transition* (ed. D. Arnal & R. Michel), pp. 489–498. Springer.
- NG, L. L. & CROUCH, J. D. 1999 Roughness-induced receptivity to crossflow vortices on a swept wing. *Phys. Fluids* **11**, 432–438.
- NITSCHKE-KOWSKY, B. & BIPPES, H. 1988 Instability and transition of a three-dimensional boundary layer on a swept flat plate. *Phys. Fluids* **31**, 786–795.
- RADEZTSKY, R. H., REIBERT, M. S. & SARIC, W. S. 1994 Development of stationary crossflow vortices on a swept wing. *AIAA Paper* 94-2373.
- RADEZTSKY, R. H., REIBERT, M. S. & SARIC, W. S. 1999 Effect of isolated micron-sized roughness on transition in swept-wing flows. *AIAA J.* **37**, 1370–1377.
- RADEZTSKY, R. H., REIBERT, M. S., SARIC, W. S. & TAKAGI, S. 1993 Effect of micron-sized roughness on transition in swept-wing flows. *AIAA Paper* 93-0076.
- REED, H. L. & SARIC, W. S. 1989 Stability of three-dimensional boundary layers. *Annu. Rev. Fluid Mech.* **21**, 235–284.
- REIBERT, M. S., SARIC, W. S., CARRILLO, R. B. & CHAPMAN, K. L. 1996 Experiments in nonlinear saturation of stationary crossflow vortices in a swept wing boundary layer. *AIAA Paper* 96-0184.
- SARIC, W. S. 1994 Low-speed boundary-layer transition experiments. In *Transition: Experiments, Theory & Computations* (ed. T. C. Corke, G. Erlebacher & M. Y. Hussaini), pp. 1–114. Oxford University Press.
- SARIC, W. S., CARRILLO, R. B. & REIBERT, M. S. 1998 Nonlinear stability and transition in 3-D boundary layers. *Meccanica* **33**, 469–487.
- SARIC, W. S. & YEATES, L. G. 1985 Generation of crossflow vortices in a three-dimensional flat-plate flow. In *Laminar Turbulent Transition* (ed. V. V. Kozlov), pp. 429–437. Springer.
- SPALART, P. R. 1993 Numerical study of transition induced by suction devices. In *Near-Wall Turbulent Flows*, pp. 849–858. Elsevier.
- TAKAGI, S. & ITOH, N. 1994 Observations of traveling waves in the three-dimensional boundary layer along a yawed cylinder. *Fluid Dyn. Res.* **14**, 167–189.
- ZHIGULYOV, V. N. & TUMIN, A. M. 1987 *Origin of Turbulence*. Novosibirsk, Nauka (in Russian).